Acta Astronautica 220 (2024) 478–494

Contents lists available at ScienceDirect

Acta Astronautica

journal homepage: www.elsevier.com/locate/actaastro

Review article

Reflective and transmissive solar sails: Dynamics, flight regimes and applications☆

Samuel M. Thompson *,1, Nishanth Pushparaj 2, Chantal Cappelletti 2

University of Nottingham, Coates Building, University Park, Nottingham, NG7 2RD, Nottinghamshire, UK

ARTICLE INFO

Keywords:
Solar sail
Refractive
Diffractive
Transmissive
LEO
Space debris
ISAM

ABSTRACT

Refractive and diffractive solar sails have been cited to yield benefits in both performance and utility over reflective sails, but their range of viable flight regimes and future applications have not been fully explored. In this paper, a flight model is developed to test and compare these *transmissive* sail designs under realistic conditions. Raw performance is translated into tangible flight characteristics within a range of flight regimes, such as rate change of orbital energy and minimum operational altitude, and used to make comparison with reflective sails and contemporary thrusters. Additionally, the sensitivity of these flight characteristics to certain orbital parameters is explored when operating under either a locally optimal or simplified Sun-pointing steering law. The developed flight model focuses on solar radiation pressure, atmospheric drag and the effects of eclipse and orbital precession; locally optimal steering laws are numerically generated for every flight regime using a ray tracing-derived performance sensitivity profile. Relative to an idealised reflective sail, the sensitivity of transmissive sail performance is found to be lower for altitude, but higher for orbital inclination. High performance transmissive sail designs are found to outperform idealised reflective ones in every flight regime nonetheless. Meanwhile, only certain lower performance designs demonstrate this trait; others retain advantage only within high inclination, low altitude orbits. 36 m^2 transmissive sails performing an orbit-raising manoeuvre from low Earth orbit are shown to generate transit times comparable to mid-range electric thrusters. In light of these findings, potential applications for transmissive sails are discussed, as well as several practical considerations and potential limitations.

1. Introduction

Conventional 'reflective' solar sails are a relatively new yet well understood technology that are suited to a narrow band of niche applications, such as space exploration. Despite providing lower rates of acceleration than their contemporaries, they may reach higher velocities (achieve higher 'ΔV') because they do not require propellant. Optical degradation effects aside, a solar sail may accelerate indefinitely, and can be said to have infinite ΔV. Additionally, the performance of a solar sail scales directly with its size. It has been theorised that large solar sails may be manufactured from orbit using in-space additive manufacturing (ISAM) methods [1], allowing for rates of acceleration comparable to chemical engines. Conversely, conventional propulsion systems see depreciating gains in acceleration and ΔV when they are scaled up, as described by the *Tsiolkovsky rocket equation*. Solar sails can also provide continuous albeit low torque for attitude control [2,3]; they are not reliant on propellant as thrusters are, do not become 'saturated' as reaction wheels do, and can operate beyond low Earth orbit (LEO) where magnetorquers would cease to operate [4]. However, solar sails are rarely considered to be a valid choice for modern satellites, for which LEO and geosynchronous orbit (GEO) are the dominant flight regimes. This lack of demand – and the resulting absence of commercial off-the-shelf (COTS) solar sails – may be explained by the following:

1. *Rate of Acceleration*: while solar sail acceleration scales with size, the size of sail that can be launched is limited. As such, modern solar sails only generate low, *non-impulsive* rates of acceleration. Meanwhile, space missions have a time limit because satellite systems have a shelf-life. Within LEO, missions are expected to last for 2–15 years (4–5 years average) [5]. Therefore, if the ΔV

☆ This document is the result of a research project funded by the Engineering and Physical Sciences Research Council (EPSRC).
* Corresponding author.
E-mail addresses: Samuel.Thompson@nottingham.ac.uk (S.M. Thompson), Nishanth.Pushparaj@nottingham.ac.uk (N. Pushparaj), Chantal.Cappelletti@nottingham.ac.uk (C. Cappelletti).
1 Ph.D Mechanical Engineering candidate, Nottingham Geospatial Institute (NGI).
2 Assistant Professor in Aerospace Engineering, Faculty of Engineering.

https://doi.org/10.1016/j.actaastro.2024.04.032
Received 18 January 2024; Received in revised form 15 March 2024; Accepted 17 April 2024
Available online 20 April 2024

requirements of the mission can be met by a rapidly accelerating *impulsive* system, there is little reason to use a solar sail.

2. *Sensitivity to Altitude and Inclination*: the large surface area of a solar sail will induce significant atmospheric drag when exposed to incoming airflow in a LEO. The sail membrane may also be deformed by the airflow, degrading its ability to generate velocity-wise SRP, exacerbating this issue. At lower altitudes, atmospheric drag will dominate SRP and induce orbital decay. For reflective sails in LEO, it is often necessary to significantly expose the sail to airflow in order to generate velocity-wise SRP (see Section 2.3); as such, they cannot operate at altitudes lower than approximately 600 km under mean solar activity, and experience degraded performance below about 1000 km [6,7]. This is a significant disadvantage, as the majority of satellites carry out their missions entirely within LEO [8]. Furthermore, solar sail performance is lower in low inclination orbits (see Section 2.4). Because LEO missions often constitute a rideshare or 'piggyback' launch whereby multiple satellites (each with their own desired injection orbit) are launched together, the injection orbit parameters of individual satellites may be compromised. As a solar sail will be incompatible with some orbits, their inclusion may restrict the launch opportunities of the satellite developer [9].
3. *Sensitivity to Solar Cycle*: in LEO, solar sail performance and minimum operational altitude are highly sensitive to solar activity. This is because heightened solar activity correlates with increased EUV (extreme ultraviolet) radiation, which heats the thermosphere and causes atmospheric density to rise. Atmospheric density, and therefore atmospheric drag, may change by an order of magnitude above the expected median as a result, albeit in a predictable manner [10].
4. *Model Uncertainties*: sail performance is difficult to model accurately as non-linearities may be introduced by billowing, wrinkling, material deformation, satellite self-shadowing and optical degradation [2,11–14]. Additionally, uncertainties are presented by both the optical properties of a sail [15] and the expected solar irradiance [15,16].
5. *Impingement on Other Systems*: the presence of a solar sail can affect several unrelated systems. Self-shadowing affects solar panels, antennas and optical payloads directly. Self-shadowing (and sail emission) will also cool a satellite, indirectly affecting temperature-sensitive systems such as batteries and biological payloads [17]. Furthermore, the performance of a solar sail depends on its orientation (or 'attitude') relative to the Sun [2], which must be maintained continuously so as to not lengthen the already lengthy manoeuvre times [18,19]. This can conflict with the operation of other systems that require pointing.
6. *Deployment*: any system that involves moving parts is viewed with suspicion by satellite developers as they introduce single points of failure [20] and deployment systems are amongst the most complex. Additionally, solar sails have been shown to promote vibration under insufficient tension [21]. Sufficient tension during deployment is particularly difficult to achieve for large sails and, left unchecked, may result in membrane drift that may jam a deployment mechanism [22].

Transmissive solar sails, which include *refractive* and *diffractive* sails, may mitigate many of these issues through the mechanisms discussed in this paper. This may endear them to a wider range of satellite applications that could benefit from 'infinite' ΔV. Potential benefits cited in existing literature include greater velocity-wise solar radiation pressure [23–30], significant improvements in LEO performance [23], lower minimum operational altitudes [23] and reduced mission complexity through simplified steering [28,29]. In particular, the aforementioned issues of (1) acceleration and (2) sensitivity to altitude (but not inclination) may be notably improved as explored in Section 5; to a lesser extent, (4) model uncertainties, (5) impingement on other systems and (6) deployment may be benefited by transmissive design, as explored in Section 6.

Overall, this paper seeks to collate and expand upon the existing literature pertaining to transmissive solar sails. Design proposals have been made for such sails [23–30], but their performances have not been compared with one another previously. In particular, their individual performances were generally not applied to a realistic flight model (FM) to calculate tangible flight characteristics, such as rate change of orbital energy or minimum operational altitude under the effects of atmospheric drag, eclipse and precession. In one exception, minimum altitude was ascertained [23], but only for a single instance for which eclipse and precession could be reasonably neglected. In another, optimal transit times were explored for two interplanetary transfers [28], but the aforementioned effects were not considered as each transit began from a heliocentric orbit.

Applying the performance of these sails to a realistic FM enables an evaluation of the sensitivity of sail behaviour to various orbital parameters and flight regimes. This is important because non-heliocentric orbits are rarely optimal for solar sailing and – as explored in Section 4.2 – such orbits will generally precess into one that is sub-optimal anyway. Furthermore, understanding the extent to which these sails are suited to non-heliocentric orbits is crucial when exploring the role of these sails within contemporary 'Earth-centric' satellite applications. To ensure that these sails are properly steered, locally optimal steering laws are generated numerically for every flight regime; this is also used to make a comparison with sails steered under a Sun-pointing ('zero-α') steering law, which is a simplified and often-cited steering law within transmissive sail literature [23,25,29,30].

In this paper, the first principles of solar sailing are explored in a manner applicable to both conventional and transmissive solar sails. This serves as a basis for the evaluation of different sail designs — in particular, their suitability for various flight regimes and applications, and how they compare with the 'baseline' reflective sail. A perfect specular reflector is chosen as this baseline so as to not obfuscate the comparison with transmissive sail designs, which are themselves idealised to varying degrees; this also ensures that newer sails are not advantaged by having less literature pertaining to their inefficiencies. To further contextualise performance, transmissive sails are later compared with contemporary thrusters performing an orbit-raising manoeuvre under identical conditions.

2. Solar sailing principles

This section provides a mathematical framework by which different kinds of solar sail may be modelled, assessed and compared.

2.1. Solar radiation pressure

Photons have momentum p, which is expressed in terms of the Planck constant h and photon wavelength λ_k. In vector form $\mathbf{p}$, this is expressed by the reduced Planck constant $\hbar = \frac{h}{2\pi}$ and the wave vector $|\mathbf{k}| = \frac{2\pi}{\lambda_k}$ wherein $\hat{\mathbf{k}}$ acts perpendicular to the wavefront, the direction of propagation in vacuum (Eqs. (1)–(2)) [31].

$$p = \frac{h}{\lambda_k} \tag{1}$$

$$\mathbf{p} = \hbar\mathbf{k} = \frac{h}{\lambda_k}\hat{\mathbf{k}} \tag{2}$$

Solar radiation pressure (SRP) arises because photon momentum may be transferred to a particle should the two interact. Typically, many millions of photons will contribute to SRP at a given instance. The SRP vector $\mathbf{P_S}$ is the accumulation of these momentum transfers per unit time dt, per unit area dA, and may be expressed in terms of the mean impulse per interaction $\bar{\Delta\mathbf{p}}$ and the mean number of interactions per second $\bar{N}$ [32]. The resultant optical force $\mathbf{F_S}$ may be expressed as the mean $\bar{\mathbf{P}}_\mathbf{S}$ applied over a given area A (Eq. (3)–(4)):

$$\mathbf{P_S} = \sum_{i=1}^{N} \frac{\Delta \mathbf{p}(i)}{\mathrm{d}t} = \bar{N}\bar{\Delta \mathbf{p}} \tag{3}$$

$$\mathbf{F_S} = \int\int_A \mathbf{P_S} \cdot dA = \bar{\mathbf{P}}_\mathbf{S} A \tag{4}$$

A more convenient approach is to express incident photons as *irradiance* (colloquially, 'illumination'): the incident radiated power upon an illuminated surface ($\mathrm{W/m^2}$). In the case of a solar sail at 1 au (*astronomical unit*), this is described by the solar constant $G_{SC} = 6.674\ \mathrm{Nm^2/kg^2}$. Here the term G_{SC}/c is analogous to the rate of momentum transferred from incident photons at any given instant ($\mathrm{kg\ m/s^2}$), where $c = 299,792,458\ \mathrm{m/s}$ is the speed of light. For distances other than 1 au, radiation energy dilution due to the inverse-square law must be accounted for by dividing by the square of the magnitude of Sun vector $\mathbf{S}$ (au) (Eq. (5)). Furthermore, in the case of a flat particle – such as a sail – the illuminated area will be effectively reduced according to the *cosine* of the solar incidence angle α [33–35] (Eq. (6)):

$$\bar{\mathbf{P}}_\mathbf{S} \propto \frac{G_{SC}}{cS^2} A \tag{5}$$

$$\mathbf{F_S} \propto \frac{G_{SC}}{cS^2} A\cos(\alpha) \tag{6}$$

To complete the expression, the *type* of photon interaction must be known. Broadly speaking, these interaction types are *absorption*, *reflection* and *transmission*. In the case of absorption, photons are destroyed and all of their momentum is transferred linearly to the particle such that $\mathbf{F}_{\mathbf{S}_{\text{absorb}}}$ acts opposite to the light source unit vector $\hat{\mathbf{S}}$ (Eq. (7)) [2]. During reflection or transmission, photons are not destroyed, and a reaction force is generated that opposes their change in momentum during the interaction [34].

In the reflection case, a distinction must be drawn between *specular* and *diffuse*: in the specular case, this change in momentum acts along the particle *normal* unit vector $\hat{\mathbf{n}}$ in accordance with the *law of reflection*, and so the force $\mathbf{F}_{\mathbf{S}_{\text{reflect}}}$ acts opposite to $\hat{\mathbf{n}}$; the component of photon momentum parallel to the sail is unchanged while the component perpendicular to it is reversed, changing by twice its original value (Eq. (8)) [36]. In the presence of surface roughness, *diffuse* reflection occurs and the force $\mathbf{F}_{\mathbf{S}_{\text{diffuse}}}$ acts in both $-\hat{\mathbf{S}}$ and $-\hat{\mathbf{n}}$ in a 3:2 ratio (Eq. (9)) [37].

Finally, for transmission – which encompasses both *refraction* and *diffraction* – the SRP force $\mathbf{F}_{\mathbf{S}_{\text{transmit}}}$ is expressed in terms of the incoming and outgoing photons (Eq. (10)) [34]. The distinction between each force and the corresponding direction of outgoing photons ($\hat{\mathbf{k}}_{\text{reflect}}$, $\hat{\mathbf{k}}_{\text{diffuse}}$, $\hat{\mathbf{k}}_{\text{transmit}}$) is illustrated by Fig. 1.

$$\mathbf{F}_{\mathbf{S}_{\text{absorb}}} = -\frac{G_{SC}}{cS^2} A\cos(\alpha)\hat{\mathbf{S}} \tag{7}$$

$$\mathbf{F}_{\mathbf{S}_{\text{reflect}}} = -\frac{2G_{SC}}{cS^2} A\cos^2(\alpha)\hat{\mathbf{n}} \tag{8}$$

$$\mathbf{F}_{\mathbf{S}_{\text{diffuse}}} = -\frac{G_{SC}}{cS^2} A\cos(\alpha)\frac{3\hat{\mathbf{S}} + 2\hat{\mathbf{n}}}{\|3\hat{\mathbf{S}} + 2\hat{\mathbf{n}}\|} \tag{9}$$

$$\begin{aligned} \mathbf{F}_{\mathbf{S}_{\text{transmit}}} &= -\frac{G_{SC}}{cS^2} \|\hat{\mathbf{k}}_{\text{transmit}} - \hat{\mathbf{S}}\| A\cos(\alpha)\frac{\hat{\mathbf{k}}_{\text{transmit}} - \hat{\mathbf{S}}}{\|\hat{\mathbf{k}}_{\text{transmit}} - \hat{\mathbf{S}}\|} \\ &= -\frac{G_{SC}}{cS^2} A\cos(\alpha)(\hat{\mathbf{k}}_{\text{transmit}} - \hat{\mathbf{S}}) \end{aligned} \tag{10}$$

The latter expression is unique in that it requires a consideration of the outgoing ray unit vector $\hat{\mathbf{k}}_{\text{transmit}}$. This will depend on the geometry and properties of the particle, and can be derived by sequential applications of *Snell's law* (for refraction) [34] or the *grating equation* (for diffraction) [27] according to the number of boundaries passed by the incident photons.

In the event that each of these mechanisms occurs simultaneously, the total force is given by Eq. (11) wherein Φ_a, Φ_r, Φ_d and Φ_t are

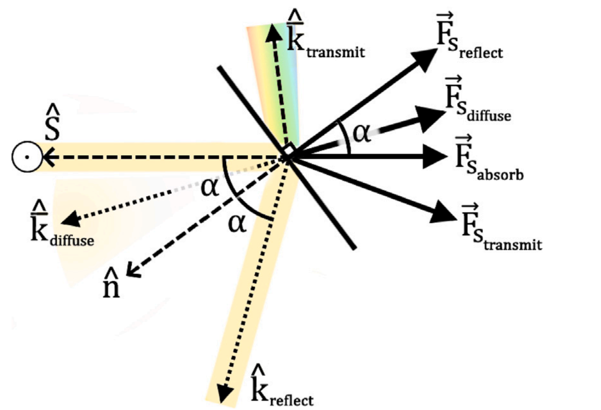

Fig. 1. SRP force components arising from absorption, (Specular) reflection, diffuse (Reflection) and transmission (refraction and/or diffraction).

the proportions of power distributed to absorption, specular reflection, diffuse reflection and transmission, respectively ($\Phi_a + \Phi_r + \Phi_d + \Phi_t = 1$).

$$\mathbf{F_S} = \Phi_a \mathbf{F}_{\mathbf{S}_{\text{absorb}}} + \Phi_r \mathbf{F}_{\mathbf{S}_{\text{reflect}}} + \Phi_d \mathbf{F}_{\mathbf{S}_{\text{diffuse}}} + \Phi_t \mathbf{F}_{\mathbf{S}_{\text{transmit}}} \tag{11}$$

2.2. Reference frames

How SRP affects a sail in orbit will depend on its attitude, position and velocity, and so the relevant reference frames must be established. Let $\mathcal{T}_B(O; \hat{\mathbf{x}}_\mathbf{B}, \hat{\mathbf{y}}_\mathbf{B}, \hat{\mathbf{z}}_\mathbf{B})$ be the 3D body-fixed reference frame originating from a solar sail centroid O, whereby the sail normal $\hat{\mathbf{n}}$ emerges from the illuminated side, is related to $\hat{\mathbf{x}}_\mathbf{B}$ by $\hat{\mathbf{x}}_\mathbf{B} = -\hat{\mathbf{n}}$, and where the yz plane represents an idealised sail surface. For reflective sails, the direction of $\hat{\mathbf{y}}_\mathbf{B}$ is arbitrary. For transmissive sails, $\hat{\mathbf{y}}_\mathbf{B}$ is chosen to be the direction of the component of SRP that is tangential to the sail (see Section 2.5). In both cases, $\hat{\mathbf{z}}_\mathbf{B}$ is defined by mutual orthogonality with $\hat{\mathbf{x}}_\mathbf{B}$ and $\hat{\mathbf{y}}_\mathbf{B}$ forming a right-handed frame. Additionally, let $\hat{\mathbf{S}}$ represent the Sun unit vector, the direction of the Sun with respect to the satellite position, and $\hat{\mathbf{p}}$ the primer unit vector, the optimal direction of impulse for a given manoeuvre; in general, $\hat{\mathbf{p}}$ describes the optimal direction of impulse for a manoeuvre to minimise transit times [38,39], or to maximise the rate change of a certain orbital parameter [7,33], depending on the steering law used (see Section 2.3). During an ideal manoeuvre, $\hat{\mathbf{x}}_\mathbf{B}$ and $\hat{\mathbf{y}}_\mathbf{B}$ will always remain within a plane bound by $\hat{\mathbf{S}}$ and $\hat{\mathbf{p}}$. It is therefore convenient to confine the analysis to this 2D Solar-primer plane $\mathbf{Sp}$, and define the 2D body-fixed reference frame $\mathcal{T}_B(O; \hat{\mathbf{x}}_\mathbf{B}, \hat{\mathbf{y}}_\mathbf{B})$ and the 2D primer or 'manoeuvring' reference frame $\mathcal{T}_\mathbf{p}(O; \hat{\mathbf{x}}_\mathbf{p}, \hat{\mathbf{y}}_\mathbf{p})$ — for which $\hat{\mathbf{p}} = \hat{\mathbf{x}}_\mathbf{p}$. For the non-ideal case wherein the attitude control fails to confine $\hat{\mathbf{n}} = -\hat{\mathbf{x}}_\mathbf{B}$ and $\hat{\mathbf{y}}_\mathbf{B}$ within the solar-primer, forces in $\mathcal{T}_B$ can be projected onto the solar-primer for use within $\mathcal{T}_b$ and the out-of-plane components can be neglected. These two reference frames can be transformed between via a rotation by angle δ about $\hat{\mathbf{q}} = \hat{\mathbf{x}}_\mathbf{B} \times \hat{\mathbf{p}}$ (Eq. (12)) as depicted by Fig. 2.

$$\delta = 90 - \arccos\left(\frac{\hat{\mathbf{x}}_b \cdot (\hat{\mathbf{p}} \times \hat{\mathbf{S}})}{|\hat{\mathbf{x}}_b|\,|(\hat{\mathbf{p}} \times \hat{\mathbf{S}})|}\right) \tag{12}$$

$$\begin{bmatrix} \hat{\mathbf{x}}_b \\ \hat{\mathbf{y}}_b \end{bmatrix} = R_{\hat{q}}(\delta) \begin{bmatrix} \hat{\mathbf{x}}_B \\ \hat{\mathbf{y}}_B \end{bmatrix}$$

Three more angles can be drawn on $\mathbf{Sp}$ in addition to $\alpha = \angle\, \hat{\mathbf{S}}\hat{\mathbf{n}}$ as depicted in Fig. 3: the angle *sail deviation* $\beta = \angle\, \hat{\mathbf{x}}_\mathbf{b}\hat{\mathbf{x}}_\mathbf{p}$, which relates the satellite attitude in $\mathcal{T}_b$ to the desired direction of impulse $\hat{\mathrm{p}}$ in $\mathcal{T}_\mathbf{p}$; *effective sail deviation* $\beta^* = \angle\, \mathbf{F_S}\hat{\mathbf{x}}_\mathbf{p}$, which determines the direction of SRP relative to $\hat{\mathrm{p}}$; and the *solar misalignment* $\gamma = \angle\, \hat{\mathbf{x}}_\mathbf{p}\hat{\mathbf{S}}$, which describes

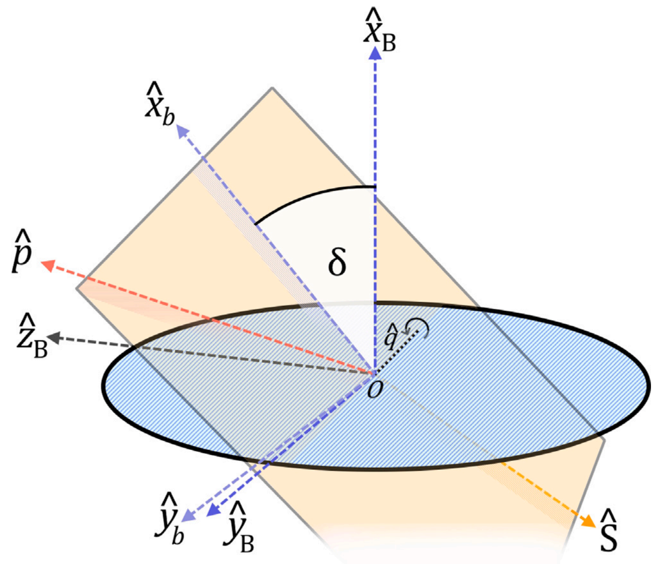

Fig. 2. 3D body-fixed reference frames rotated onto the solar-primer $\mathbf{Sp}$.

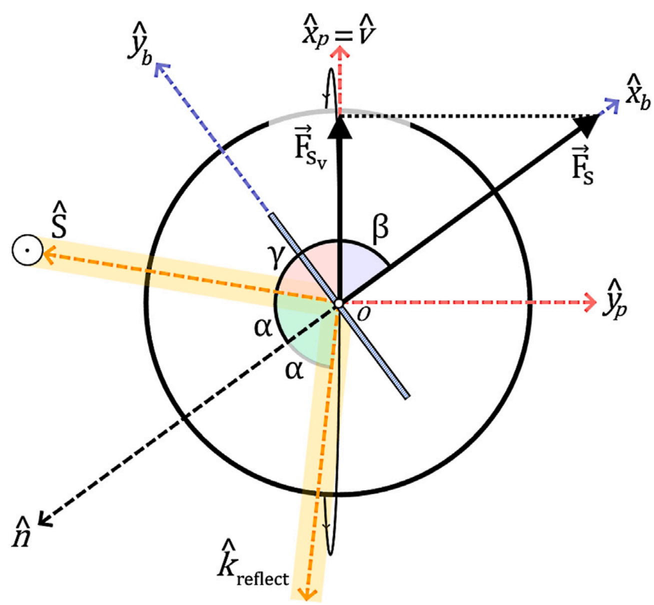

Fig. 3. 2D body-fixed reference frame in the solar-primer plane, applied to a (Specular) reflective solar sail wherein $\mathbf{F}_{\mathbf{S}_{\mathbf{x_p}}} = \mathbf{F}_{\mathbf{S}_v}$ (Orbit-raising manoeuvre).

how suitable the position of the Sun is for the desired manoeuvre at a given instant. These angles do not exist independently of one another, and it may be observed from Fig. 3 that these comply with Eq. (13). In the $\gamma = 90°$ scenario, Eq. (13) simplifies to Eq. (14). This is a notable special case that is archetypal of solar sailing flight, and is therefore frequently referenced by this paper:

$$\forall \gamma \in \mathbb{R} \rightarrow \qquad \alpha + \beta + \gamma = 180° \tag{13}$$

$$\gamma = 90° \rightarrow \qquad \beta = 90 - \alpha \rightarrow \qquad \cos(\beta) = \sin(\alpha) \tag{14}$$

However, these expressions do not feature β^* at all. As described in Eq. (15), the relationship between this angle and the other three will vary depending on the mechanism of SRP generation, making it unique. These relationships are derived from Eq. (7)–(10) (see Section 2.1) and Eq. (13):

$$\beta^* = \begin{cases} 180 - \gamma & & = f(\gamma) & \text{if absorptive} \\ \beta & = 180 - \gamma - \alpha & = f(\alpha,\gamma) & \text{if reflective} \\ \beta + f(\alpha) & = 180 - \gamma - \alpha + f(\alpha) & = f(\alpha,\gamma) & \text{if transmissive} \end{cases} \tag{15}$$

Some noteworthy features of β^* are highlighted by the above. Firstly, in each case, β^* may be expressed as a function of α, γ or both. In the absorption case, β^* is independent of sail attitude. In the reflective case, β^* has a linear relationship with sail attitude ($\beta^* = \beta$). In the transmissive case, an undefined function $f(\alpha)$ influences β^* that is specific to the sail, due to the material and micro-geometry dependence of transmissive SRP that is described in Section 2.1.

With the relationship between $\mathcal{T}_b$, $\mathcal{T}_\mathrm{p}$ and $\hat{\mathbf{S}}$ established, it is useful to split the SRP force vector $\mathbf{F_S}$ into orthogonal components. In the body-fixed frame $\mathcal{T}_b$, these components are the sail normal $\mathbf{F}_{\mathbf{S}_{\mathbf{x_b}}}$ and sail tangential $\mathbf{F}_{\mathbf{S}_{\mathbf{y_b}}}$; in the manoeuvring frame $\mathcal{T}_\mathrm{p}$, these components are transverse $\mathbf{F}_{\mathbf{S}_{\mathbf{x_p}}}$ and longitudinal $\mathbf{F}_{\mathbf{S}_{\mathbf{y_p}}}$.

Typically, raw sail performance data expresses $\mathbf{F_S}$ components in terms of $\mathcal{T}_b$. However, it is more useful to express $\mathbf{F_S}$ in terms of $\mathcal{T}_\mathrm{p}$ because this pertains directly to performance within a manoeuvre; in this frame, transverse $\mathbf{F}_{\mathbf{S}_{\mathbf{x_p}}}$ and longitudinal $\mathbf{F}_{\mathbf{S}_{\mathbf{y_p}}}$ may be called the 'useful' and 'wasteful' components. The wasteful component can be neglected, and the useful component may be derived from a raw force vector or $\mathcal{T}_b$ performance data using the expressions in Eq. (16):

$$\mathbf{F}_{\mathbf{S}_{\mathbf{x_p}}} = F_S\cos(\beta^*)\hat{\mathbf{x}}_\mathbf{p} = F_S\cos[\arccos(\frac{F_{S_{y_b}}}{F_S}) + (90-\gamma)]\hat{\mathbf{x}}_\mathbf{p} \tag{16}$$

Eq. (7)–(10) can be transcribed to the $\mathcal{T}_\mathrm{p}$ reference frame to express $\mathbf{F}_{\mathbf{S}_{\mathbf{x_p}}}$ for each mechanism (Eq. (17)–(20)).

$$\mathbf{F}_{\mathbf{S}_{\mathbf{x_p}\mathrm{absorb}}} = \frac{G_{\mathrm{SC}}}{cS^2}A\cos(\alpha)\cos(\beta^*)\hat{\mathbf{x}}_\mathbf{p} \tag{17}$$

$$\mathbf{F}_{\mathbf{S}_{\mathbf{x_p}\mathrm{reflect}}} = \frac{2G_{\mathrm{SC}}}{cS^2}A\cos^2(\alpha)\cos(\beta^*)\hat{\mathbf{x}}_\mathbf{p} \tag{18}$$

$$\mathbf{F}_{\mathbf{S}_{\mathbf{x_p}\mathrm{diffuse}}} = \frac{G_{\mathrm{SC}}}{5cS^2}A\cos(\alpha)[3\cos(\alpha+\beta^*) + 2\cos(\beta^*)]\hat{\mathbf{x}}_\mathbf{p} \tag{19}$$

$$\mathbf{F}_{\mathbf{S}_{\mathbf{x_p}\mathrm{transmit}}} = \frac{G_{\mathrm{SC}}}{cS^2}\|\hat{\mathbf{k}}_{\mathrm{transmit}} - \hat{\mathbf{S}}\|A\cos(\alpha)\cos(\beta^*)\hat{\mathbf{x}}_\mathbf{p} \tag{20}$$

Wherein specular and diffuse reflection share the β^* definition for reflection of Eq. (15). The question then becomes the nature of $\hat{\mathbf{x}}_\mathbf{p}$, which depends upon the manoeuvre being carried out and the steering law being used. Because orbit-raising manoeuvres are both simple and ubiquitous, the analysis will focus on these hereafter.

2.3. Steering law and optimal attitude

A steering law dictates how a satellite will carry out a manoeuvre; an optimal steering law aims to carry out the manoeuvre in the shortest time. One such law is the *globally optimal* steering law, which is rigorous and suitable for complex manoeuvres [28,40]. However, it also poses two-point boundary problems that require computationally expensive solving techniques, such as the shooting method [41]. The Q-law algorithm is an advanced variant of *locally optimal steering law* that has similar capabilities, is suitable for non-impulsive applications, and that can be solved analytically [42,43]. However, by focusing on the orbit-raising of a solar sail within an approximately circular orbit, a simpler locally optimal steering law will suffice. This law only aims to maximise the rate of change of a specific orbital parameter, but has nonetheless been shown to yield near-optimal transit times for many manoeuvres [7]. Applied to an orbit-raising manoeuvre, this law will aim to maximise the *rate change* of the orbital *semi-major axis* $\dot{a}$ (half the diameter of an orbital ellipse). This has been shown to be equivalent to maximising the *rate change* of *orbital specific energy* $\dot{\epsilon}$ (Eq. (21)–(22)) [7,33], which may be used to form the locally optimal steering law axiom (Eq. (23)). Through application of Eq. (15), α is presented as the sole control variable, making these expressions convenient for a numerical search (note that γ and altitude h are not control variables):

$$\dot{\epsilon} = v\dot{v} = \frac{v}{m}(F_{S_v} - D) \tag{21}$$

$$\max_{\alpha} \dot{\epsilon}(\alpha, \gamma, h) = \frac{v(h)}{m}(F_{S_v}(\alpha_{\text{opt}}, \gamma) - D(\alpha_{\text{opt}}, \gamma, h)) \tag{22}$$

$$\operatorname*{argmax}_{\alpha} \dot{\epsilon}(\alpha, \gamma, h) \equiv \operatorname*{argmax}_{\alpha} \dot{a}(\alpha, \gamma, h) = \alpha_{\text{opt}} \tag{23}$$

Where v is velocity, $\dot{v}$ is acceleration, D is the atmospheric drag force and α_{opt} is the solar incidence that maximises $\dot{\epsilon}$; h and γ can be said to compose an instance of a flight regime by confining the analysis to circular, 1 au orbits. By adjusting α, the locally optimal steering law will seek to maximise the component of net force that is acting in $\hat{\mathbf{v}}$. It can therefore be said that the primer unit vector is $\hat{\mathbf{x}}_{\text{p}} = \hat{\mathbf{v}}$.

Eq. (21)–(23) presents α as the sole control variable through application of Eq. (15). These expressions are convenient, but they occlude the nature of the problem. A more natural depiction is provided by Eq. (24), which highlights that the problem is actually a balancing of the three *controllable* solar sailing angles α, β and β^*:

$$\max_{\alpha} \dot{\epsilon}(\alpha, \beta, \beta^*, h) = \frac{v(h)}{m}(F_{S_v}(\alpha_{\text{opt}}, \beta^*) - D(\beta, h)) \tag{24}$$

This form is useful for understanding the nature of α_{opt} by highlighting the individual contributions of each control angle to $\dot{\epsilon}$. For example, α dictates sail illumination and is an argument of F_S, while β^* defines the alignment of $\mathbf{F_S}$ with $\hat{\mathbf{v}}$ and is an argument of the ratio $\lambda = F_{S_v}/F_S$. When atmospheric drag is present, β represents the angle relative to the incoming airflow and $|\beta| - 90°$ determines the magnitude of drag force D (drag is minimised when $\beta = \pm 90°$). At a given instance wherein h is considered constant, these contributions can be made clearer yet by Eq. (25):

$$\dot{\epsilon} \propto F_{S_v}(\alpha, \beta^*) - D(\beta) = F_S(\alpha)\lambda(\beta^*) - D(\beta) \tag{25}$$

2.4. Flight regimes

$\{h, \gamma\}$ can only describe a single instance in time. During orbit-raising by solar sail, an orbit that begins as circular will generally remain circular because they are non-impulsive. It is therefore convenient to confine the subsequent analyses to circular orbits for our purposes such that h can be said to be constant over the duration of a single orbit. On the other hand, γ generally cycles between some minimum value and some maximum value as a function of true anomaly ν (orbital angular position), albeit always with a mean of $\bar{\gamma} = 90°$ (see Section 4.2). The variable γ is said to belong to the continuous set S_γ (Eq. (26)). Additionally, we introduce the Sun-*orbit* angle Γ as the angle between the *specific relative angular momentum unit vector* $\hat{\mathbf{h}}$ (the orbital plane *normal vector*) and $\hat{\mathbf{S}}$. This is the sole argument of S_γ:

$$\gamma(\nu, \Gamma) \in \mathrm{S}_\gamma(\Gamma) \tag{26}$$

$$\mathrm{S}_\gamma(\Gamma) = [\textsc{min}\,\gamma, \textsc{max}\,\gamma] = \{\gamma(\nu, \Gamma) \in \mathbb{R} | \textsc{min}\,\gamma \le \gamma \le \textsc{max}\,\gamma\} \tag{27}$$

$\{h, S_\gamma\}$ can be said to compose a flight regime, and naturally, some flight regimes are more optimal than others. Consider two reflective sails in orbits of arbitrary h wherein one is an ecliptic plane LEO of $\Gamma = 90°$ (Eq. (28)), and the other is a 'sunrise-sunset' polar LEO of $\Gamma = 0°$ (Eq. (29)):

$$\mathrm{S}_\gamma(90°) = \{\gamma(\nu, 90°) \in \mathbb{R} | \quad 0° \le \gamma \le 180°\} \tag{28}$$

$$\mathrm{S}_\gamma(0°) = \{\gamma(\nu, 0°) \in \mathbb{R} | \quad 90° \le \gamma \le 90°\} \tag{29}$$

A low-resolution assessment of these flight regimes can be made by making S_γ discrete and attributing it a sample size of four (each sample representing a quarter of an orbit). For clarity, we can assume that $\nu = 0°$ when $\gamma = 180°$ for both, and assign corresponding sets for

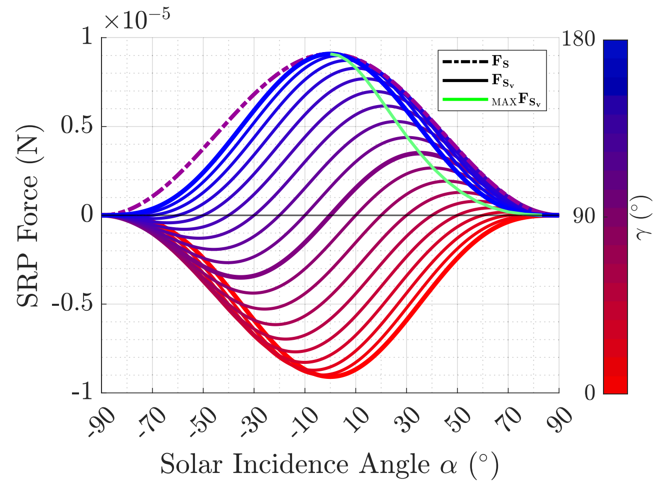

Fig. 4. 1×1 m^2 Reflective sail SRP force-α profiles for $0° \le \gamma \le 180°$ ($\gamma = 0$, 90, 180° are thickened).

position $\nu \in \mathrm{S}_\nu$ and optimal solar incidence $\alpha_{\text{opt}} \in \mathrm{S}_{\alpha_{\text{opt}}}$. Note that atmospheric drag is neglected for this example (Eq. (30)):

$$S_\nu(90°) = \{0, 90, 180, 270\} \qquad S_\nu(0°) = \{0, 90, 180, 270\}$$

$$S_\gamma(90°) = \{180, 90, 0, 90\} \qquad S_\gamma(0°) = \{90, 90, 90, 90\} \tag{30}$$

$$S_{\alpha_{\text{opt}}}(90°) = \{0, \text{NaN}, 90, 35.26\} \qquad S_{\alpha_{\text{opt}}}(0°) = \{35.26, 35.26, 35.26, 35.26\} \tag{31}$$

In each instance, α_{opt} is the solar incidence that achieves maximum F_{S_v}. For a reflective sail in a perfect vacuum, this means maximising the product of $\cos(\alpha)^2$ (the modifier of F_S) and $\cos(\beta^*)$ (the modifier of ratio $\lambda = F_{S_v}/F_S$) (see Eq. (17), (25)). To demonstrate the relationship between γ, α and the available SRP, SRP-α profiles for $90° < \gamma < 180°$ are presented in Fig. 4. Finally, the efficiency set $S_{\eta_{S_v}}$ can be defined, wherein η_{S_v} represents the F_{S_v} as a percentage of the maximum possible F_{S_v} (at 1 au) through specular reflection (Eq. (32)–(33)):

$$\eta_{S_v} = 100 \times \frac{F_{S_v}}{(\frac{2G_{\text{SC}}}{c})} \tag{32}$$

$$S_{\eta_{S_v}}(90°) = \{100, 0, 0, 38.51\} \qquad S_{\eta_{S_v}}(0°) = \{38.51, 38.51, 38.51, 38.51\} \tag{33}$$

In the first case ($\Gamma = 90°$), the flight regime is defined by an oscillation between optimal and sub-optimal conditions due to the shifting γ; at $\nu = 0°$ the Sun is *retrograde* to sail motion ($\gamma = 180°$) and both trigonometric terms are maximised perfectly by $\alpha_{\text{opt}} = 0°$, which is the maximum SRP configuration (depicted by Fig. 5). The flight conditions at this attitude yield 100% of the theoretical maximum F_{S_v}. At $\nu = 180°$ (the other side of the orbit), the Sun is *prograde* to motion ($\gamma = 0°$) and $\alpha_{\text{opt}} = 90°$; this is the zero SRP configuration, and it is optimal because any SRP generated would cause the sail to decelerate. Conversely, at the two intermediary points ($\nu = 90, 270°$) the Sun is perpendicular to motion ($\gamma = 90, 90°$). The optimal solution is arbitrary at the first intermediary point because the sail is eclipsed by the Earth (see Section 4.3). At the second intermediary point, the product of the trigonometric terms is maximised by $\alpha_{\text{opt}} = 35.26°$, which is a *tacked* configuration.

In the second case ($\Gamma = 0°$), the flight regime is defined by a constant $\gamma = 90°$, yielding the same tacked $\alpha_{\text{opt}} = 35.26°$ configuration as before, but for the entire orbit. This places the average efficiency of the orbit (for reflective solar sailing) at 38.51%. Conversely, averaged across all four samples, the efficiency of the first case flight regime is

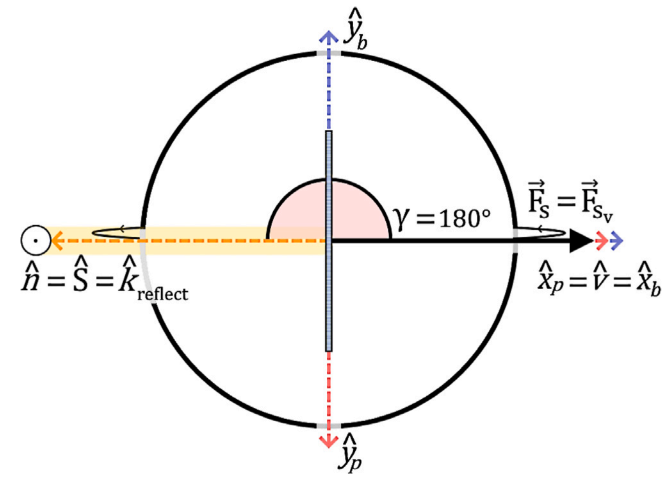

Fig. 5. Ecliptic LEO (at $\gamma = 0°$) for a reflective solar sail with atmospheric drag neglected.

34.63%. Clearly, the constant γ second case is more optimal. Incidentally, this unchanging $\gamma = 90°$ flight regime is qualitatively identical to that of a circular heliocentric orbit.

If atmospheric drag is not neglected, the efficiency discrepancy will grow as h is reduced, favouring the second case. This is in part because, in the first case, the attitude that a sail must adopt to maximise SRP when the Sun is *retrograde* is also the maximum drag configuration; there are also segments of the orbit (e.g. the *prograde* Sun region) for which acceleration is impossible. This is exacerbated by eclipse, which in the first case, becomes more prominent as h is reduced. Conversely, the second case maintains a lower drag, tacked configuration throughout, can accelerate constantly, and experiences zero eclipse (at least initially — see Section 4.3).

2.5. Introduction to transmissive solar sails

Transmissive solar sails differ from reflective ones in terms of their mechanisms for generating SRP and their behaviour within the various flight regimes. These mechanisms are mentioned in brief in Section 2.1.

Transmissive solar sails transmit and redirect incident sunlight through a transparent, often highly refractive membrane to generate SRP. This SRP can be generated even at $\alpha = 0°$ by harnessing surface microstructures that act as waveguides or gratings [23–27,29,30,44–48]. Whether the primary SRP mechanism of the membrane is refraction or diffraction depends on the dominant spectrum of light that the membrane is designed to transmit (usually the visible spectrum), and the scale of the microstructures that this light is transmitted through. If the smallest element of these microstructures is an order of magnitude greater than the longest wavelength of said spectrum, refraction will be the primary mechanism; if the microstructures are similarly sized to the wavelengths of said spectrum, diffraction must be considered [49]. Crucially, the SRP force vector $\mathbf{F_S}$ is not aligned with $\hat{\mathbf{x}}_\mathbf{B}$ (which aligns with the sail normal $\hat{\mathbf{n}}$) for a transmissive sail. This is in contrast to specular reflective sails, for which $\mathbf{F_S} = \mathbf{F}_{\mathbf{S}_{\mathbf{x_b}}}$. Instead, it will have a significant $\mathbf{F}_{\mathbf{S}_{\mathbf{y_b}}}$ component that acts tangential to the sail [23,25,26,29]. As depicted by Fig. 6, the tangential component $\mathbf{F}_{\mathbf{S}_{\mathbf{y_b}}}$ will tend to align with the useful transverse component $\mathbf{F}_{\mathbf{S}_{\mathbf{x_p}}}$ while in a nearly Sun-pointing, $\alpha \approx 0°$ attitude under near-optimal, $\gamma \approx 90°$ conditions.

This means that a transmissive sail may not need to be tacked at all, allowing it to maximise illumination (maximise $\mathbf{F_S}$) without sacrificing β^* and the ratio $\lambda = F_{S_v}/F_S$. Furthermore, within an optimal orbit, this Sun-pointing attitude will coincide with the minimum drag configuration ($\beta = 90°$). In short, the priorities discussed in Section 2.3 do not necessarily conflict for transmissive sails as they do for reflective ones; to a degree that is afforded by the flight regime, they can often be satisfied simultaneously. The reduced drag under optimal conditions also enables transmissive sails to operate at lower altitudes [23], which is explored in greater detail in Section 5.2.

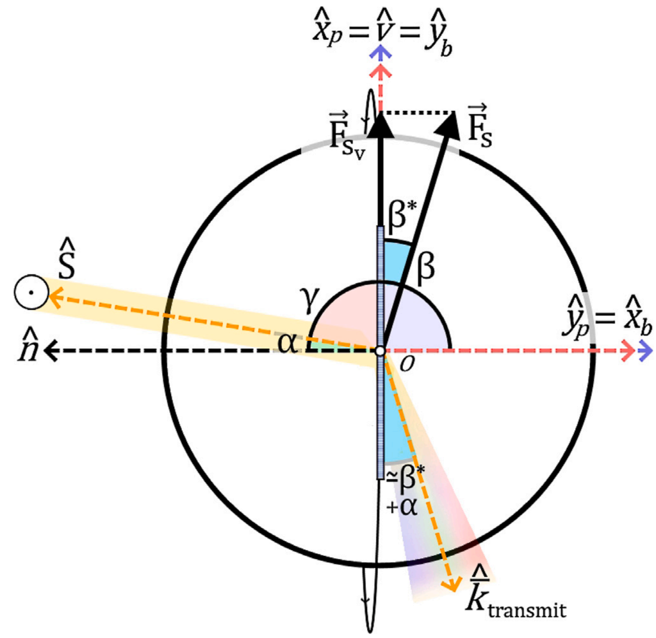

Fig. 6. Transmissive sail at $\gamma \approx 90°$.

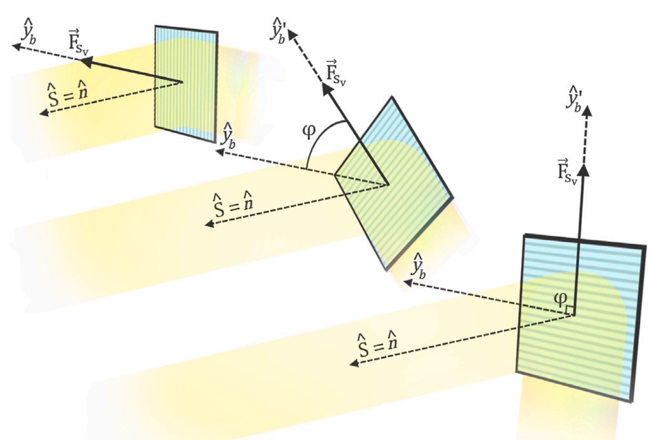

Fig. 7. Transmissive sail with $\mathbf{F}_{\mathbf{S}_v}$ Locked to $\hat{\mathbf{y}}$.

Although the magnitude of $\mathbf{F}_{\mathbf{S}_{\mathbf{y_b}}}$ changes with α, its direction is generally constant. As depicted by Fig. 7, a transmissive sail may alternate between an orbit-raising, orbit-lowering or out-of-plane manoeuvre simply by changing its roll angle ϕ while remaining in a Sun-pointing, $\alpha = 0°$ attitude. Some transmissive sail designs have also been proposed to be capable of providing both passive or active Sun-pointing stability [23,24,30,47,50]. Under optimal conditions, these phenomena may allow for greatly simplified steering when compared with reflective sails. For certain interplanetary transits, the cumulative effects of improved F_{S_v} and simplified steering have been suggested to yield reductions in transit times of 30-44% [28].

However, the behaviour of different transmissive sails will also vary significantly according to their microstructure and mechanism for generating SRP. It is therefore difficult to make assertions about transmissive sails as a breed, without neglecting the many exceptions. To this end, transmissive sail designs from various proposals are evaluated, beginning with an overview in Section 3.2. Because these proposals are generally interested in maximum sail performance, certain unknowns have not been addressed by them. The first is the question of operational flexibility, and whether the advantages of transmissive sails remain valid for sub-optimal orbits. If they do not, this would restrict their potential applications. This question is answered in Section 5. Other unknowns that pertain to the practical side of operating transmissive sails (e.g. materials, mass efficiency) are explored more briefly in Section 6.

3. Analysis of transmissive solar sail proposals

This section details and compares existing transmissive sail proposals. To facilitate their evaluation, this begins with the defining of the parameters by which they may be initially compared, which a focus on their performance under ideal conditions. Analysis of these sails under non-ideal conditions is carried out in Section 5.

3.1. Scalar performance parameters

Eqs. (34)–(35) characterises η_S and η_{S_v}, which are the percentage incident solar irradiance that is converted to SRP and *transverse* SRP, respectively. Eq. (36) describes λ, which is the transverse force ratio. Both η_{S_v} and λ have been expressed before in some form, but are reiterated here for clarity. Note that all parameters that are sensitive to flight regime assume $\gamma = 90°$ at 1 au ($G_{SC} = 1370\ \mathrm{W/m^2}$), and that $\textsc{max}\ F_S = 2G_{SC}/c$:

$$\eta_{S_v} = \frac{F_{S_v}}{\text{MAX} F_S} \tag{34}$$

$$\eta_S = \frac{F_S}{\text{MAX} F_S} \tag{35}$$

$$\lambda = \cos(\beta^*) = \frac{F_{S_v}}{F_S} \tag{36}$$

Since reflective sails are used as the baseline for comparison, it is convenient to express the efficiencies of transmissive sails not in terms of percentage irradiance converted, but in proportion to the theoretical maximum efficiencies of reflective ones. Relative efficiencies, denoted by an asterisk, are expressed by Eq. (37)–(38). Note that η^*_S is expressed to highlight that its relative and absolute forms are indistinguishable, because the $\textsc{max}\ F_S$ that a reflective sail can achieve is theoretically 100% of $2G_{SC}/c$:

$$\eta^*_S = \frac{F_S}{\text{MAX} F_S} = \frac{F_S}{\left(\frac{2G_{SC}}{c}\right)} = \eta_S \tag{37}$$

$$\eta^*_{S_v} = \frac{F_{S_v}}{\text{MAX} F_{S_v}} \tag{38}$$

3.2. Transmissive sail proposals

Developments in the field of study of refractive and diffractive solar sails have lead to myriad designs. The performance data of these designs has been collated and converted to use the scalar performance parameters described in Section 3.1; these are tabulated in Table 1.

These designs can be roughly partitioned by performance and conformity with the transmissive sail archetype described in Section 2.5. High performance sails demonstrate greater transverse acceleration than the reflective baseline with $\eta^*_{S_v} > 100\%$, while archetypal ones are said to demonstrate a force ratio of $\lambda > 0.5$. Notably, all high performance sails are archetypal, but some of the lower performance sails are not.

High performance, 'Type A' variants include the refractive rotated lightfoil [24], refractive gradient-index waveguide [29], diffractive Littrow transmission [25] and diffractive prism grating [27] sails. Sails within this category tend to outperform reflective sails in every flight regime (see Section 5). Type A sails also tend to be *metasails* — sails with membranes composed of metamaterials. The rotated lightfoil sail is an exception, being a non-metasail with very high performance that could reasonably be fabricated via double-sided nanoimprinting lithography processes (non-rotated lightfoils may be fabricated with conventional nanoimprinting, but such a sail would generate zero net SRP at $\alpha = 0°$).

Conversely, the Sun-facing transmission [26] variant is a metasail that belongs to 'Type B': it is lower performance but still archetypal (and in this case, notable for featuring the highest λ of any design). Type B sails, of which the refractive prism array [23] is the only other example, tend to outperform reflective sails only within a narrow band of flight regimes (see Section 5).

The lower performance, non-archetypal, 'Type C' variants include the diffractive Littrow reflection [25], bi-grating [45] and liquid crystal [30] sails. The former is not truly transmissive, and has superficial behavioural similarities to a reflective sail. However, it diffracts sunlight in such a way as to gain no benefit from tacking; its force vector is always locked to $-\hat{\mathbf{S}}$ (which for $\gamma = 90°$ is the longitudinal axis $\hat{\mathbf{y}}_{\mathbf{p}}$). This behaviour is a hindrance here, but may have application within artificial Lagrange points or certain laser-driven sail configurations. The latter two are notable for generating a significant component of force in the sail normal $\hat{\mathbf{x}}_{\mathbf{b}}$ (indicated by their high η_S but low λ). This sometimes plays to their advantage in later analyses (see Section 5) as, paired with a suitable steering law, they may exhibit behaviours similar to either the reflective or transmissive sail archetype, depending on which mode is most beneficial at the time. In general, they tend to outperform their low performance, archetypal peers, and outperform or match the performance of reflective sails (see Section 5).

Finally, it should be noted that each author applies different assumptions, simplifications and modelling techniques. Many proposals also offer a spectrum of possible designs, and in these cases, the data transcribed represents just one of a number of possibilities. Furthermore, while scalar performance parameters allow for easy 'at a glance' comparisons of sail designs, they do not account for the potential benefits of simplified steering and, in some cases, active control of λ that may be achieved by certain designs [23,25,30]. They also pertain only to a single ($\Gamma = 0°$) flight regime. To explore the behaviour of these sails under more realistic and varied conditions, a LEO FM is developed. This is applied to assess the suitability of these sails to various flight regimes and applications.

Table 1
Scalar performance parameters of solar sails at $\gamma = 90°$, conversion of approximate data transcribed or extracted from figures of tabulated sources.

Category	Mechanism	α (°)	η_{S_v} (%)	$\eta^*_{S_v}$ (%)	η_S (%)	λ
Reflective	Specular reflection	35.26	38.49	100	81.65	0.471
		0	0	0	100	0
Diffractive	Littrow reflection [25]	0	0	0	100	0
	Littrow transmission [25]	35.26	39.00	101.33	47.43	0.822
	Sun-facing transmission [26]	20	24.73	64.24	27.17	0.910
		0	21.50	55.86	23.12	0.930
	Bi-grating beam rider [45]	0	28.00	72.75	100	0.280
	Liquid crystal [30]	0	25.00	64.95	93.41	0.268
	Prism grating [27]	0	43.50	113.02	50.42	0.863
Refractive	Lightfoil (50° Rotation) [24,47]	0	50.00	129.90	64.03	0.781
	Prism array [23]	0	20.16	52.39	24.70	0.816
	Gradient-index waveguide [29]	0	45.14	117.29	58.12	0.777

4. Flight model

First we define the metrics used to evaluate these sails within the model:

1. 'Local performance' or rate change of specific orbital energy $\dot{\epsilon}(h,\gamma)$: Eq. (21) (J/kg s)
2. Optimal solar incidence angle $\alpha_{\text{opt}}(h,\gamma)$: Eq. (23) (°)
3. Performance 'breakpoint' altitude $h_{\text{break}}(h,\gamma)$: the altitude (km) at which the $\dot{\epsilon}$ of a transmissive sail and the reflective baseline sail are equal (if any).
4. Minimum operational altitudes, instantaneous $h_{\min}(\gamma)$, transient $h_{\min^*}(\Gamma)$, stable $h_{\min^{**}}(i)$: the minimum altitudes (km) at which a sail achieves $\dot{\epsilon} > 0$ J/kg s over different timescales.
5. Orbit-raising time $t_{h_1\to h_2}(h,i)$: the time taken (months) to accelerate from a circular orbit of altitude h_1 to one of altitude h_2.

4.1. Modelling LEO flight

The atmosphere is modelled as a free-molecule airflow, and all perturbative forces other than velocity-wise SRP F_{S_v} and atmospheric drag D are assumed to be negligible (aerodynamic lift is neglected). This yields Eq. (39) and a simplified form given by Eq. (40).

$$\begin{aligned}\dot{\epsilon} &= \frac{v}{m}A(F_{S_v} - D)\\ &= \frac{v}{m}A\left(\frac{2G_{\text{SC}}}{cS^2}\cos^2(\alpha)\cos(\beta^*) - \frac{1}{2}\rho v^2 C_D\right) \quad (39)\\ &= \frac{v}{m}A\left(\eta^*_{S_v\,\text{MAX}}F_{S_v} - \frac{1}{2}\rho v^2 C_D\right) \quad (40)\end{aligned}$$

The remaining unknowns – the air density ρ and the coefficient of drag C_D – are calculated using a model provided by source [51] (Eq. (41)–(42)), wherein h (km) is the altitude:

$$\begin{aligned}\rho &= 3.91\times10^{-9}\exp(-0.01841h)\\ &\quad + 1.304\times10^{-11}\exp(-0.009264h) \quad (41)\\ C_D &= 2\sigma_n\frac{v_w}{v}\cos^2(\beta) + \frac{2}{\sqrt{\pi}}\frac{v_a}{v_s}[(2-\sigma_n)\cos^2(\beta) \quad (42)\\ &\quad + \sigma_t\sin^2(\beta)\exp(-(\frac{v_s}{v_a})^2\cos^2(\beta))]\\ &\quad + 2(2-\sigma_n)[\cos^2(\beta) + \frac{1}{2}(\frac{v_a}{v_s})^2 + \sigma_t\sin^2(\beta)]\end{aligned}$$

Additionally, the calculation of C_D requires an approximation of the ambient and sail surface molecule speeds v_a and v_w (Eq. (43)–(44)), as well as the normal and tangential momentum accommodation coefficients σ_n and σ_t (Eq. (45)) [51]:

$$v_a = 1089\exp(-0.000604h) + 22.72\exp(0.004959h) \quad (43)$$

$$\frac{v_w}{v} \approx 0.05 \quad (44)$$

$$\sigma_n \approx \sigma_t \approx 0.8 \quad (45)$$

4.2. Generating S_γ and modelling a dynamic Γ

As explored in Section 2.4, a satellite in a circular Earth-centred orbit that is described by Γ will encounter a range of γ denoted by set S_γ. The sole exception to this is the $\Gamma \in \{0, 180°\}$ sunrise–sunset polar orbit, for which a constant $\gamma = 90°$ is (initially) experienced.

In order to provide the FM with S_γ, orbits are generated in 3D space and propagated to ascertain each $\gamma(\nu,\Gamma)$ numerically. Initial orbits are generated with the ascending node offset by 90° from 'aphelion' (closest point to the Sun); when varying the *initial* orbits, changes in Γ are achieved by changing orbital inclination i exclusively (never rotating the orbital nodes), such that $\Gamma = 90 - i$. The range of γ experienced by several of these initial orbits is demonstrated by Fig. 8a. It can be seen that for each orbit, the mean is always $\bar{\gamma} = 90°$, while the spread between MIN γ and MAX γ varies more substantially by orbit (generally, a greater spread implies a less optimal orbit for solar sailing).

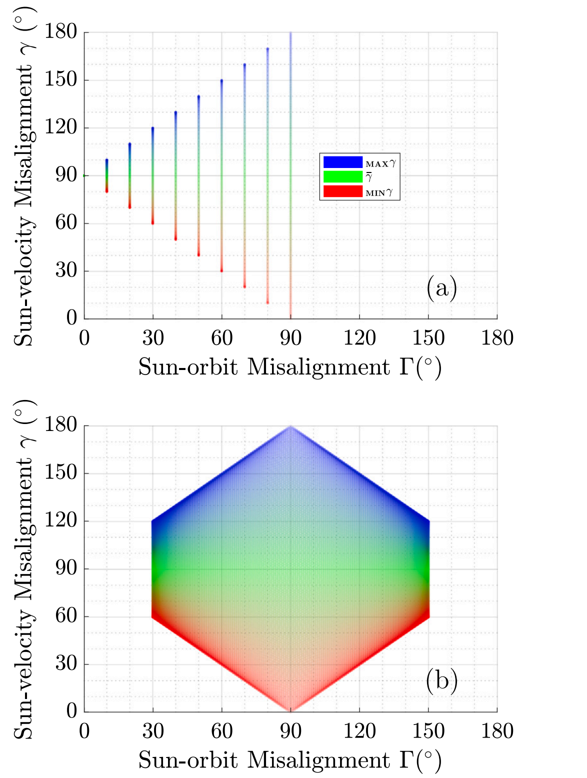

Fig. 8. (a) S_γ versus Γ for 'initial' orbits of $\Gamma \in \{0, 10, 20\ldots 90\}$ (sample size lowered for clarity) wherein $i = 90 - \Gamma$. (b) Time-variant S_γ versus Γ for an initial $\Gamma = 30°$, $i = 60°$ orbit.

It is also necessary to acknowledge that the Γ of a typical non-heliocentric orbit is not constant; Γ will change because the Sun vector $\hat{\mathbf{S}}$ rotates relative to an Earth satellite's orbital plane as a symptom of Earth's own heliocentric orbit, and because the orbital plane itself will rotate due to the J2 perturbation [52]. A dynamic Γ implies a dynamic range S_γ, and because solar sailing manoeuvres will generally be executed over many months, the S_γ of the orbit may change many times over. This may cause an orbit to oscillate between being optimal and sub-optimal for solar sailing. As an example, Fig. 8b demonstrates this variation for an initially $\Gamma = 30°$ orbit. These time-variant S_γ sets are generated for each orbit by rotating the orbital plane about an Earth-centred ecliptic normal axis in intervals (i = constant). To reduce the number of profiles that need to be generated, axial tilt is neglected; heliocentric Earth and J2 are said to cause rotation about the same axis (in reality, J2 acts about the Earth's axis of rotation [52], which has 23.4° obliquity with the ecliptic normal). These profiles are cycled through by the FM at a rate that is dictated by the current $\dot{\Gamma}(i,h)$ and the time elapsed (see Eq. (46)–(48)):

$$\begin{aligned}\dot{\Gamma}(i,h) &= \dot{\Gamma}_S + \dot{\Gamma}_{J2}(i,h) \quad (46)\\ \dot{\Gamma}_S &= \frac{360}{T_{\text{Earth}}} = \frac{360}{(365\times24\times60^2)} = 3.1536\times10^7\ °/\text{s} \quad (47)\\ \dot{\Gamma}_{J2}(i,h) &= -\frac{3}{2}\text{J2}\left(\frac{r_E}{h+r_E}\right)^2\sqrt{\frac{\mu}{(h+r_E)^3}}\cos(i)\frac{180}{\pi} \quad (48)\end{aligned}$$

Wherein J2 = 1.08262668×10^{-3}. It is noteworthy that $\dot{\Gamma}_S$ is independent of orbital parameters, while $\dot{\Gamma}_{J2}(i,h)$ may be selected by controlling them. This brings about a special case known as a Sun-synchronous orbit (SSO), wherein both arguments of $\dot{\Gamma}$ are equal and opposite and $\dot{\Gamma} = 0°$/s (see Eq. (49)–(50)):

$$\begin{aligned}\dot{\Gamma}_{J2}(i_{\text{SSO}}(h),h) &= -\dot{\Gamma}_S \quad (49)\\ i_{\text{SSO}} &= \arccos\left(-\frac{2}{3}\times\frac{360}{365\times24\times60^2}\right. \quad (50)\end{aligned}$$

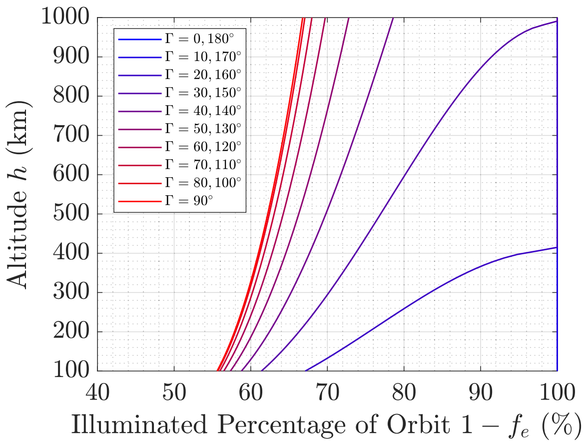

Fig. 9. Illuminated orbit fraction $1 - f_e$ versus Altitude h for a Range of Γ (note that $\Gamma \leq 10°$, $\Gamma \geq 170°$ curves are superimposed at $1 - f_e = 100\%$).

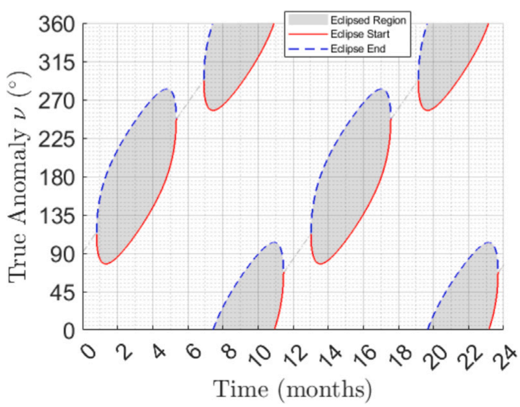

Fig. 10. Changing eclipse region due to a shifting Γ arising from relative sun position and the J2 perturbation ($h = 550$ km polar orbiter).

$$\times \frac{\pi}{180} \times \frac{1}{\mathrm{J2}} (\frac{h + r_E}{r_E})^2 \sqrt{\frac{(h + r_E)^3}{\mu}})$$

Because an SSO negates dynamic-Γ effects, a 'dusk–dawn' SSO is in reality often more optimal than a sunrise–sunset polar orbit, particularly for manoeuvres that span many months.

4.3. Eclipse

Solar sails in most permutations of LEO are affected by eclipses (see Fig. 9). These produce a periodic cessation of any positive $\dot{\epsilon}$, which in turn may erode the propagated performance of the sail in terms of $t_{h_1 \rightarrow h_2}$ and minimum operational altitudes $h_{\min^*}$ and $h_{\min^{**}}$. For a given altitude h, a circular orbit will only encounter an eclipse if the Sun-orbit angle Γ is smaller than a certain *eclipse angle* Γ_e (Eq. (51)) [53]:

$$\Gamma_e = \arcsin(\frac{r_E}{r_E + h}) + 90 \tag{51}$$

If an eclipse will occur, the percentage of an orbit for which a satellite is eclipsed is described by the eclipse factor f_e (Eq. (52)) [53]:

$$f_e = \begin{cases} \frac{1}{180} \arccos \frac{\sqrt{h^2 + 2 r_E h}}{r_E + h \cos(\Gamma - 90)} & \text{if } |\Gamma| < \Gamma_e \\ 0 & \text{if } |\Gamma| \geq \Gamma_e \end{cases} \tag{52}$$

Naturally, there is a range of h and Γ for which eclipse will *never* occur (for example, altitudes at $\Gamma \leq 10$; see Fig. 9). Furthermore, $\dot{\Gamma}$ has a significant effect on eclipse fraction f_e due to the relationship highlighted in Eq. (52). For example, a sunrise–sunset polar orbit will eventually precess into a 'noon–midnight' orbit, and then back again. This effect is highlighted by Fig. 10 (sunrise–sunset is depicted by the zero-eclipse region; noon–midnight is depicted by the points at which the eclipse region is tallest).

Furthermore, it should be noted that perfectly flat sails are assumed by this model and, because $|\alpha| \leq 90°$ is ensured by attributing these sailcraft with absolute control authority, the issue of self-shadowing is negated entirely. However, real solar sails are subject to imperfect steering, membrane deformations and occlusion from both the satellite bus and the sail support structures, resulting in self-shadowing effects. This may be particularly severe in low LEO where membrane deformation is elevated by air flux, and in orbits with demanding steering profiles. Lastly, while a binary 'on-off' eclipse is a convenient approximation that does not significantly effect simulation results, in reality the effect is more gradual.

4.4. Generating locally optimal steering laws

The final hurdle for evaluating solar sails is ensuring that each is controlled in-flight optimally. For the reflective solar sail, the locally optimal steering law is determined numerically by solving for α_{opt} via Eq. (22)–(23), (39), yielding the steering law shown by Fig. 11a.

The steering laws of transmissive sails are not so easily derived. A simple Sun-facing $\alpha_{\text{opt}} = 0°$ steering law may suffice for optimal $\gamma = 90°$ orbits, but transmissive solar sails are greatly disadvantaged when this law is applied to other orbits. To maintain equity, true locally optimal $\alpha_{\text{opt}} = f(h, \gamma)$ steering laws are required.

To generate them, α-F_{S_v} profiles are needed for each transmissive sail. Because these are not formulaic as for reflective sails, and because these data sets are not readily available, these profiles are generated through a custom optical simulation using a methodology based on source [34]. To remain within scope, the developed simulation focused on refraction, dispersion and reflection by a single-index material; absorption and diffuse reflection are ignored on the assumption that these sail materials are smooth, highly transmissive, and that these mechanisms therefore contribute little to SRP. In particular, neglecting diffuse reflection substantially speeds up simulation times [54]. This simulation is applied to generate α-F_S and α-β^* profiles for a microprism array sail of dimensions akin to its original proposal [23]. This data was used as the generic model for transmissive sail sensitivity to α: the profile was normalised as a percentage of its $\alpha = 0°$ value and multiplied by the scalar performance parameters of each sail proposal to generate analogous α-F_S and α-β^* profiles, which in turn were used to generate analogous α-F_{S_v} performance profiles. Therefore, the performance at $\alpha = 0°$ was preserved by these analogs, but their idiosyncratic behaviours across the full γ range were only approximated by the generic model. In particular, the active λ control proposed by the liquid crystal sail [30] may attribute it a flatter sensitivity profile than this model suggests. Nevertheless, most transmissive sail designs demonstrate very similar behaviours within their proposal, such as a slightly off-zero α_{opt}. These transmissive analog profiles were used to generate a locally optimal steering law numerically via Eq. (22)–(23), (40). An example steering law is shown by Fig. 11b. It can be seen that an optimal reflective solar sail at low altitude will exhibit an α_{opt} that tends to bring about $\beta = 180 - \gamma - \alpha = 90°$ in order to minimise drag D, and at higher altitudes, converges upon an α_{opt} that favours maximum F_{S_v} as D becomes less significant. Naturally, at $\gamma = 90°$, the reflective sail converges upon $\alpha = 35.26°$. The transmissive sails produced similar steering laws for $400 \leq h \leq 500$ km where the tendency is to minimise drag. Otherwise, the steering law curves collate into one of several divergent 'streams' arising due to non-linearities in their SRP-α sensitivity profile. These streams tend to form around peaks in the profile, which become optimal at different γ for different sails.

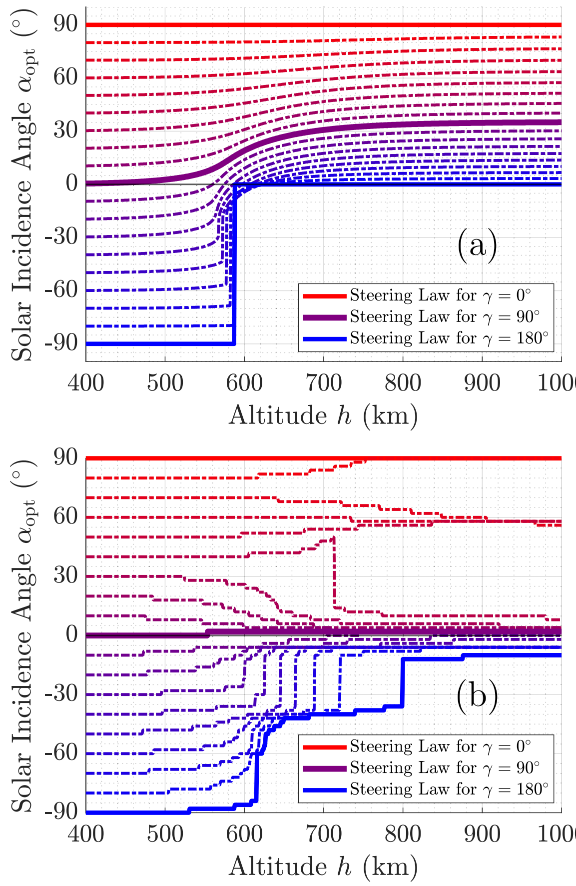

Fig. 11. LEO α_{opt} for (a) a perfect reflector and (b) a (Sensitivity analog) gradient-index waveguide solar sail, using a locally optimal steering law.

4.5. Simplified satellite bus and thruster model

Some simulations require additional parameters pertaining to the satellite itself. Satellite bus drag is assumed to be negligible, and each bus is assigned m_{bus} = 3.6 kg. It is assumed that all sails have equivalent momentum accommodation coefficients to that of a conventional solar sail $\sigma_t = \sigma_n = 0.8$ [3], and are attributed identical mass m = 1 kg and area (A = 1 m^2 unless otherwise stated). For comparison, some of these satellites are modelled with thrusters. These thrusters [55–58] are attributed equivalent dry masses to that of the sails, and are only made heavier by their wet mass. This ensures that the results are not skewed in favour of the sails by assuming that they are of significantly lower mass (in reality, they almost certainly are, but the magnitude of this discrepancy is unknown). Where not specified by a datasheet, 0.5 kg of propellant is assigned. The circular orbit assumption is maintained for all satellites, and so the *Oberth effect* is neglected.

5. Simulation and evaluation

5.1. Instantaneous performance profiles in LEO

Fixed-γ, variable-h profiles are generated for $\dot{\epsilon}$-h wherein $\Gamma = 0°, \gamma = S_\gamma = 90°$ (Figs. 12a, 13a), as well as fixed-h, variable-γ profiles for $\dot{\epsilon}$-γ wherein h = 550 km (Figs. 12b, 13b). Two simulation runs are carried out: in the first, transmissive sails operate with a zero-α steering law (Fig. 12). In the second, these use a locally optimal steering law (Fig. 13). During both runs, a reflective solar sail using a locally optimal steering law is used as a baseline.

Table 2
LEO performance parameters of idealised solar sails in a typical $\gamma = 90°$ orbit (Zero-α steering law example).

Type	Mechanism	α (°)	$\eta^*_{S_v}$ (%)	$\dot{\epsilon}_{500\text{ km}}$ (J/kg)	$\dot{\epsilon}_{1000\text{ km}}$ (J/kg)	h_{MIN} (km)	h_{break} (km)
–	Specular reflection	$\alpha(h)$	$\eta^*_{S_v}(\alpha)$	−0.004	0.007	568	–
		35.26	100	−0.028	0.007	602	–
		0	0	−0.004	0	–	–
A	Lightfoil (50° rotation)	0	129.90	0.006	0.009	446	∞
	Gradient-index waveguide	0	117.29	0.005	0.008	452	∞
	Prism grating	0	113.02	0.004	0.008	454	∞
B	Sun-facing transmission	0	55.86	0	0.004	499	635
	Prism array	0	52.39	0	0.004	503	628
C	Bi-grating beam rider	0	72.75	0.001	0.005	482	678
	Liquid crystal	0	64.95	0.001	0.005	489	656

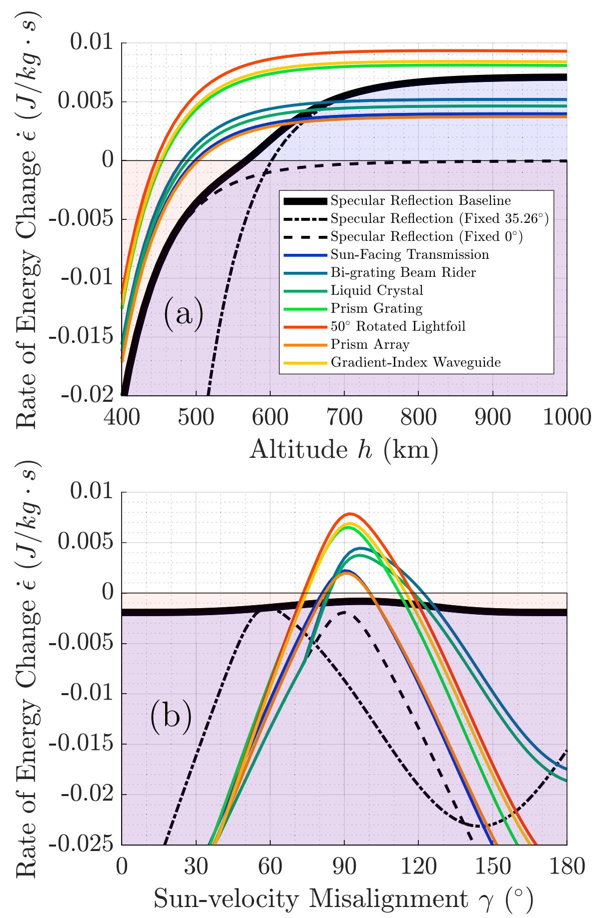

Fig. 12. Performance profiles of transmissive sails using a zero-α steering law, a reflective solar sail using a locally optimal steering law and two fixed specular reflectors in circular LEOs: (a) Fixed $\gamma = 90°$, (b) fixed h = 550 km.

Analysing the variable-h profiles first (Figs. 12a, 13a): using both steering laws, every transmissive sail outperforms the baseline at altitudes lower than h = 630 km — even those with inferior $\eta^*_{S_v}$. Notably, all transmissive sails could continue to accelerate below 505 km, in contrast to the baseline specular reflector, which could not do so any lower than 570 km. A list of minimum operational altitudes h_{MIN} is tabulated in Table 2 for the zero-α law. Notably, even lower performance transmissive sails demonstrate a range of altitudes for which they outperform the baseline reflector. This is described by $0 < h < h_{\text{break}}$. The parameter h_{break} is represented in Fig. 13 by the point at which the $\dot{\epsilon}$ curve of a sail intersects with the $\dot{\epsilon}$ curve of the baseline. Transmissive sails that have higher scalar $\eta^*_{S_v}$ outperform the baseline

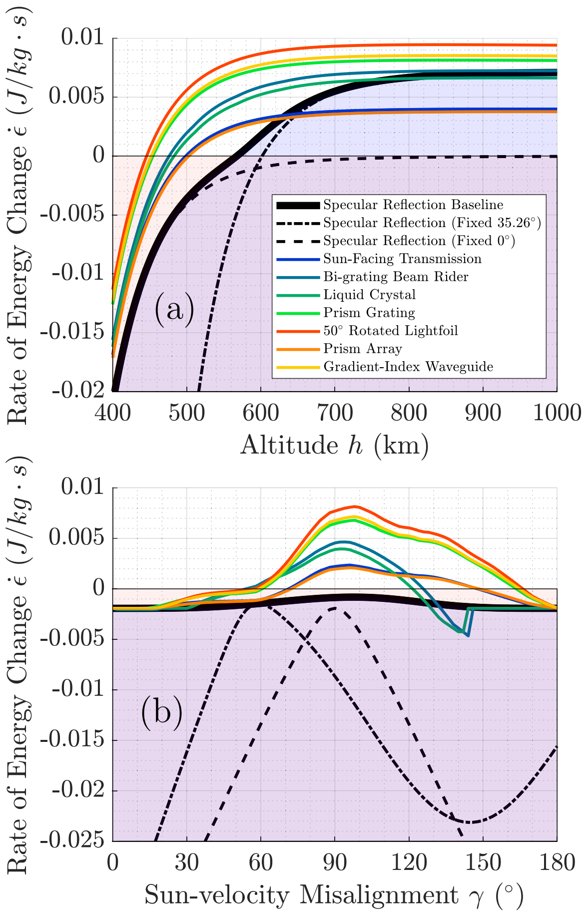

Fig. 13. Performance profiles for solar sails using a locally optimal steering law plus two fixed specular reflectors in circular LEOs: (a) Fixed $\gamma = 90°$, (b) fixed $h = 550$ km.

at every altitude, and so their curves never intersect (denoted $h_{\text{break}} = \infty$).

The two variable-h profiles are indistinguishable at lower altitudes (where the two steering laws are practically identical) but differ at high altitude. When a zero-α law is applied (Fig. 12a), the relative success of *all* solar sails at $h = 1000$ km (where drag is negligible) corresponds with the rankings of their scalar $\eta^*_{S_v}$; those with higher $\eta^*_{S_v}$ than the baseline perform better and *vice versa*. The equivalent profile that was generated with a locally optimal steering law (Fig. 13a) yields a higher $\dot{\epsilon}$ at $h = 1000$ km for transmissive sails than the zero-α equivalent. This occurs because the locally optimal steering law places these sails into a slightly off-zero-α attitude which, according to the generic sensitivity model, registers a slightly higher $\eta^*_{S_v}$ than those at zero-α. However, it is only substantial for Type C sails (e.g. bi-grating beam rider). This is because these have a large normal component to SRP and so receive a disproportionate increase in performance at high altitude when adopting a locally optimal steering law, where they benefit greatly from tacking.

A greater discrepancy may be observed between the two variable-γ profiles (Figs. 12b, 13b): the zero-α transmissive sails experience a significant erosion of performance as their γ deviates from 90°. Conversely, locally optimal transmissive sails demonstrate considerable robustness, and are able to operate at γ far beyond the optimal. Type A sails demonstrated the widest range of tenable γ for both laws. Of the lower performance sails, non-archetypal Type C variants demonstrated a wider range of tenable γ than their archetypal Type B peers when using a zero-α law. This is likely by merit of their higher $\eta^*_{S_v}$, rather than any nuanced behaviours pertaining to non-archetypes. Indeed, when using a locally optimal steering law, the lower performance, archetypal sails were more versatile than their lower performance, non-archetypal peers despite having lower $\eta^*_{S_v}$, demonstrating that archetypal, high-λ behaviour is more effective at low altitudes. Conversely, non-archetypal sails benefit greatly from tacking, and are seen to gain a larger performance increase from a locally optimal steering law than their peers when they are at high altitudes (e.g. bi-grating beam rider, Fig. 13a).

When compared with the baseline reflective sail, transmissive sails in general are shown to be less sensitive to altitude h, but *more* sensitive to γ. However, because their maximum performance is so much higher in the $h = 550$ km example, they tend to retain their advantage here for nearly the entire γ range, even when their performance declines at a faster rate.

5.2. Instantaneous, transient and stable minimum operational altitudes

To build a more comprehensive picture of the operational flexibility of these sails, minimum operational altitude profiles are generated. Minimum altitude is defined as the altitude at which $\dot{\epsilon} = 0$ J/kg s. Three minimum operational altitudes are defined to represent different timescales over which this may be achieved: *instantaneous* h_{min} represents the altitude needed to meet this condition over a single instance, depending on local conditions (single γ); *transient* h_{min^*} pertains to an entire orbital period, depending on the cumulative effect of the range of conditions experienced (single S_γ as seen in Fig. 8a); *stable* $h_{\text{min}^{**}}$ pertains to an initial orbit propagated to account for dynamic-Γ effects (time-variant S_γ as seen in Fig. 8b). Hereafter, a locally optimal steering law is employed by all actively steered sails. The *instantaneous* h_{min}-γ profiles (Fig. 14a) reveal interesting behaviours through their asymmetry. Firstly, all solar sails struggle to operate effectively when their motion is carrying them towards a *prograde* Sun (particularly for $0° \leq \gamma \leq 30°$). By a small margin, reflective and Type C transmissive sails are the most disadvantaged by these conditions. Conversely, at its extremity, the *retrograde* Sun regime favours reflective and Type C transmissive sails due to their greater ability to generate velocity-wise SRP under these conditions (enabled by their larger force component in the sail normal $\hat{\mathbf{x}}_\mathbf{b}$). The majority of the γ range ($30° \leq \gamma \leq 150°$) is dominated by transmissive sails of all varieties; of these, Type A variants demonstrate the lowest h_{min} nearly throughout.

The *transient* h_{min^*}-Γ profiles (Fig. 14b) reveal how low a solar sail can orbit without said orbit decaying. It is most pertinent to large ISAM sails which, being able to escape Earth's atmosphere rapidly, do not need to consider dynamic-Γ effects. At the optimal extremes ($\Gamma = 0, 180°$), h_{min^*} is shown to be lowest for transmissive sails (in order of their $\eta^*_{S_v}$ ranking) and highest for reflective sails. At the sub-optimal extreme ($\Gamma = 90°$), transmissive sails retain advantage but by a smaller margin. The exception to this is the Type B transmissive sails; these are shown to struggle within sub-optimal (e.g. near-equatorial) orbits, and even demonstrate a higher h_{min^*} than reflective sails. It may also be observed that in general, the h_{min^*} of these profiles never rise as high as the highest peaks of the h_{min} profile, but exhibit similar valleys. This is to be expected, as the average $\bar{\gamma}$ is always 90°; constantly optimal orbits (for which $S_\gamma = 90°$) are possible, as depicted by the identical valleys of both profiles. However, it is impossible to have an orbit that is constantly sub-optimal (e.g. no orbits can comprise only the prograde Sun regime). It is also of note that the Γ for which the eclipse fraction f_e becomes non-zero ($\Gamma = 20°$) is identifiable by a sudden increase in h_{min^*}. It is notable that this increase is more significant for transmissive sails than for the reflective baseline, which highlights an interesting behaviour: eclipse prevents acceleration from occurring during one of the two segments of an orbit for which $\alpha \approx 0°$ is tenable (the orbital segment near 'perihelion'; furthest from the Sun). These are ideal flight conditions for transmissive sails. Conversely, the *retrograde* Sun portion of these orbits marginally favour reflective sails and are never occluded.

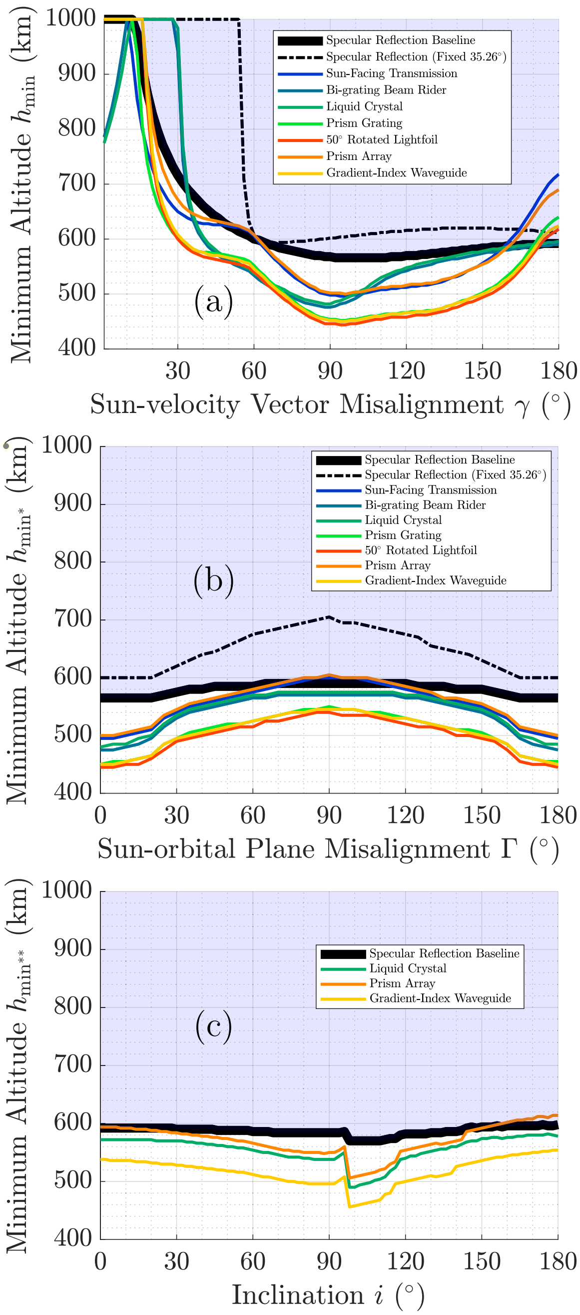

Fig. 14. Minimum operational altitudes: (a) Instantaneous h_{min} versus γ, (b) Transient h_{min^*} versus Γ, (c) Stable $h_{min^{**}}$ versus i.

The *stable* $h_{min^{**}}$-i profiles (Fig. 14c) reveal how low a solar sail can orbit when said orbit is subject to dynamic-Γ effects. This is most pertinent to modern solar sails which may take many months to escape Earth's atmosphere. Because propagating hundreds of orbits over several months is computationally expensive, only three transmissive sails were propagated; the liquid crystal, prism array and gradient-index waveguide sails are chosen to represent the Type C, B and A sails, respectively. Considering that $\Gamma = 90 - i$ for *initial* orbits, the $h_{min^{**}}$ profile largely agrees with h_{min^*}, and the relative ranking of these sails is mostly conserved. The asymmetry of this profile and the concentration of valleys around i_{SSO} is predominantly due to the J2 perturbation, the sensitivity of different orbital inclinations to it, and the subsequent effects of a dynamic-Γ (see Sections 4.2–4.3). Furthermore, for these profiles the effect of eclipse is only truly absent

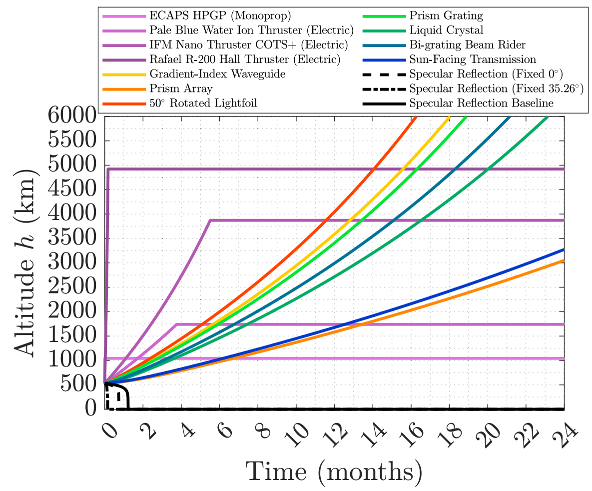

Fig. 15. Orbit-raising for thrusters and A = 36 m^2 solar sails from a h = 530 km, circular sunrise–sunset polar orbit ($\Gamma = 0°$).

at i_{SSO}, and is a significant contributor to the sharp fall in h_{min^*} that may be observed.

5.3. Propagated performance for typical manoeuvres

The final simulation explores the performance of these sails as they carry out an orbit-raising manoeuvre, and demonstrates the effects of time-variant S_γ arising from heliocentric Earth and J2 perturbation effects. Sail performance is compared with that of contemporary propulsion systems (model described in Section 4.5). Sails are assigned areas of A = 36 m^2 consistent with a 6 m square sail. Two profiles are generated for manoeuvres spanning up to 24 months, which are discussed below. The first profile (Fig. 15) depicts various satellites starting from the same injection orbit and serves to highlight the performance of medium-sized transmissive sails relative to (approximated) contemporary propulsion systems. All satellites begin from a h = 530 km, circular sunrise–sunset polar orbit ($i = 90°, \Gamma = 0°$). The $t_{h_1 \rightarrow h_2}$ for each sail and thruster is visible for any $h_1 \geq 530$ km, $h_2 \leq 6000$ km.

As expected, the reflective sails failed to perform orbit-raising from such a low altitude, which is consistent with the results of Fig. 14. The $t_{530 \rightarrow 6000\ \mathrm{km}}$ of the Type A and C transmissive sails only differed by around 20%, while Type A and B differed by nearly 100%. Relative to thrusters, the $t_{530 \rightarrow h_2}$ of these sails were greater at any h_2 for which the thrusters had not run out of fuel; as expected, larger sails would be needed to compete in terms of raw acceleration. However, the rates of acceleration for Type A and B sails were comparable to that of the mid-range electric thrusters (Pale Blue Water Ion [58] and IFM Nano Thruster [56]), though significantly outclassed by Hall effect [55] and cold gas thrusters [57] (these happen to be the highest and lowest ΔV thrusters, respectively). By merit of not requiring propellant, Type A and C transmissive sails exceeded the h_2 and ΔV of the cold gas and Hall effect thrusters as within 2.5-3.5 months and 14-20 months, respectively. If one assumes that these sails may be fabricated in an economically viable manner akin to that of a cold gas thruster, these results are encouraging, and suggest that such a sail may be favourable for many applications in both the short and long term (see Section 5.5).

The second profile focuses on a single Type A sailcraft injected into a h = 530 km circular orbit (Fig. 16a), but from various inclinations i and Sun-velocity misalignment Γ at injection. This profile serves to explore the operational flexibility of transmissive sails. Naturally, thruster satellite performance is not influenced by i or Γ. As expected, injection into an $i = 90°$ sunrise–sunset polar orbit is not truly the most efficient for solar sailing; the $i = 97.98°$ dusk–dawn SSO yields substantially higher

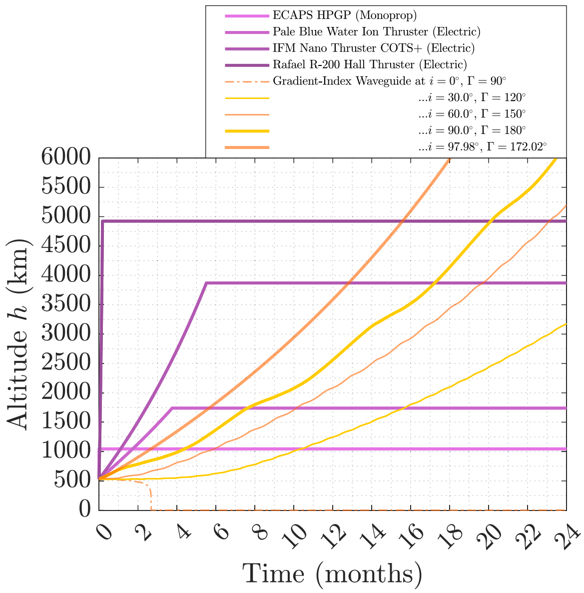

Fig. 16. Orbit-raising for thrusters and an $A = 36$ m^2 transmissive solar sail from a $h = 530$ km at various inclinations i.

dh/dt because dynamic-Γ effects are mitigated. Initially, the manoeuvre from the sunrise–sunset polar orbit *is* faster than the manoeuvre from a dusk–dawn SSO. However, J2 and heliocentric Earth effects cause the orbit to precess from sunrise–sunset to noon–midnight, which implies a less optimal S_γ and a higher eclipse fraction f_e. Eventually, this orbit returns to sunrise–sunset – and so on – leading to the 'wobbly' dh/dt of the manoeuvre (which is shared by many of the high inclination prograde orbits shown). It can be seen that at $i = 0°$, the sailcraft is unable to perform the manoeuvre from this altitude. These results demonstrate that, although the operational flexibility of these sails are considerably improved, they are inherently less flexible than modern thrusters.

5.4. Results

Relative to reflective solar sails, transmissive sails demonstrate lower sensitivity of their performance metrics to h, but greater sensitivity to i throughout; all solar sails prefer SSO and polar orbits, but this proclivity is pronounced in transmissive sails (particularly archetypal Type A–B variants). Type A and C variants generally retained advantage even within less favourable flight regimes despite this, by merit of either (A) their much higher peak performance or (C) flexibility of steering. For Type B sails, advantage over reflective sails was typically only found in low h, low i flight regimes. Furthermore, the (stable) minimum altitude advantage of transmissive solar sails over reflective ones was shown to be less substantial in non-polar and non-SSO orbits.

Relative to conventional propulsion systems, the 36 m^2 transmissive sails that were used in the case study were shown to be capable of comparable rates of acceleration to mid-range electric thrusters, but were greatly outclassed in this respect by cold gas and Hall effect thrusters. Unlike thrusters, the $t_{h_1 \to h_2}$ of solar sails was also shown to be highly sensitive to i. Naturally, all thrusters were outclassed by all transmissive sails in terms of maximum h_2 and ΔV.

5.5. Potential applications

It has been shown that transmissive sails operating in LEO may compete with contemporary propulsion systems if they are suitably sized, which implies that they may carry out a multitude of different LEO satellite missions. However, economics also plays a significant role in the choosing of satellite systems, and these sails may yet be relegated to niche applications if the assumption that they hold an economic advantage over other systems is proven to be invalid. While this is a safe assumption for some transmissive sail designs, it is more speculative for others (e.g. certain metasails).

Generally, transmissive sails may be the optimal solution for missions that entail high ΔV in LEO and the inner Solar System and, more speculatively, missions that seek to minimise cost. Missions with the greatest compatibility with transmissive sails include long-duration missions, high altitude missions, and low altitude missions in SSO. Missions with the least compatibility include those that require rapid manoeuvring, those that require operation at very low altitude, or those that begin from low inclination orbits.

In the short term, Type B or C transmissive sails composed of conventional materials could provide a low-cost solution to propulsion for small satellite developers operating in LEO and beyond. Amateur developers – who traditionally use cold gas thrusters or none – could gain access to an inexpensive, high-ΔV system, perhaps enabling amateur space probes or similar. Their simplified steering may also endear them for operation in highly atypical orbits, such as those involving 'artificial Lagrange points'. However, lacking the flexibility of the high performance variants, their operation in low LEO may be relegated to SSO and near-polar inclinations.

In the medium term, Type A or C transmissive sails predominantly composed of metamaterials could be used for a variety of contemporary applications in LEO, in a similar role to the electric thruster. This would enable greater longevity at presumably reduced cost, with the trade-off being an incompatibility with certain LEO flight regimes. Their pseudo-infinite ΔV may also be exploited for the performing of debris mitigation missions, as a transmissive sailcraft could complete multiple rendezvous-and-ferry trips between debris clouds and re-entry altitudes (albeit likely paired with a small thruster for fine-control at rendezvous). Indeed, the growing issue of space debris may see many satellite operators adopt drag sails to comply with new debris mitigation regulations (see Section 6.4), making solar sails a more attractive prospect in turn for any satellite mission.

In the long term, it is possible that sails of arbitrary size may be fabricated in space, thereby increasing acceleration to an arbitrary degree. Perhaps in an ISAM future, this could even be done economically. A large sail (or multiple small sails) could be used to ferry manned interplanetary spacecraft, or even tow mineral-rich asteroids into near-Earth orbit for exploitation. Advantage may even be found in the outer Solar System or interstellar space through the use of a 'sun-diving manoeuvre', beam-propulsion configurations, or sails of tremendous size.

6. Practical considerations

6.1. Materials

Traditionally, solar sail membranes are composed of a metallised polymer; the metallic layer carries out the optical functions, the polymer core carries out the structural functions, and both contribute to maintaining thermal equilibrium. Transmissive solar sails differ in that they must be transparent, and so eschew the metallic layer. Generally, a single material must fulfil each of the optical, structural, and thermal requirements for these sails.

In diffractive and refractive solar sail literature, sail performance has typically been the focus (for which this paper is no exception). As such, the structural and thermal requirements are often neglected, and the true suitability of the sails for spaceflight is not addressed. For example, polystyrene (PS) is often cited due to its exceptional optical properties [23,28]; furthermore, PS is helpfully resistant to space radiation [59,60]. However, it is also extremely brittle, fractures under slight elongation [61], and may be a risky venture for spaceflight if flown as a microns-thick membrane. In this case, workarounds exist that may warrant further research. For example, a PS membrane may be strategically fractured pre-flight and adhesed to a suitably transparent structural layer, thereby negating the risk of structural failure in a manner similar to that of reflective sails. PS derivatives and nanocomposites (including shape memory polymers) have also been proposed with much improved flexibility [62,63]. Furthermore, CP1 Polyimide and certain variants of polyethylene terephalate (PET/BoPET) would be less prone to failure, and may be compatible with these designs as they exhibit similar optical properties.

Conversely, many high performance transmissive sails cite metamaterials as the source of their highly desirable optical properties [25,27,29,48,64]. However, it is not yet known whether these materials can be fabricated in a scalable or economically viable manner with the desired specifications, nor whether these materials are suitable for spaceflight.

6.2. Optical degradation

Optical degradation effects are an asterisk on the proverbial '*infinite-*ΔV' of solar sails. However, predicting rates of degradation in space is, for now, an inexact science, as it occurs for a multitude of reasons including outgassing, thermal cycling [65,66], and interactions with electromagnetic (EM) radiation, corpuscle radiation [60,67,68] and atomic oxygen [60]. Every material exhibits different degrees of sensitivity to these phenomena, and each sensitivity may also vary with temperature. Furthermore, the expected degree of exposure to these phenomena is inconstant; most vary by orbit, solar activity or both. It is also difficult to predict whether a transmissive sail would suffer less from optical degradation in space by utilising single-layer, optical (meta)material films instead of multi-layered, metallised ones.

However, there is sufficient literature for speculation. For example, reflective sail optical degradation due to high-energy EM and corpuscle radiation often involves the ionisation of the metallic layer as a prominent mechanism [69,70]; organic polymers are not usually ionised by radiation [71], and would not be degraded through this mechanism. Polymers also tend to be less susceptible to damage from high-energy corpuscle or EM radiation because these forms of radiation target bonds at random (rather than selectively, as for 'low-energy' EM radiation in the UV–IR spectrum) [71]; its effects are distributed and, in some cases, may be harmlessly dissipated. Variants of polyimide and PET have been shown to tolerate high doses of this high-energy radiation before experiencing significant damage [72]. These phenomena may suggest that transmissive sails would experience a reduced rate of degradation from these sources.

On the other hand, no polymer is immune to these phenomena. With sufficiently high exposure, optical degradation will occur due to the formation and accumulation of free radicals, from the forming of conjugate double-bonds, or from polymeric unsaturation [60]. Also, while the metallic layer of a reflective sail may be prone to ionisation, it serves to protect the polymer membrane in other ways: these metallic films are generally quite reflective to UV, and highly reflective to visible and IR EM radiation. Conversely, while an optical polymer will be practically transparent to visible EM, it will be absorptive to UV and IR. In this respect, the ramifications of having no metallic layer will likely vary from polymer to polymer: some may become rapidly degraded due to the scission of certain chemical bonds arising from their selective absorption of UV; others may have mechanisms to dissipate this energy as heat or fluorescence [71], thereby delaying optical degradation.

Of particular interest is the mechanism of thermal cycling: the absorption and emission of visible and IR radiation contributes significantly to the heating and cooling of a solar sail [70]. While optical polymers are generally more absorptive to IR than metals, they are also of higher emissivity, and are generally slightly less absorptive than metals in the visible spectrum (i.e. optical polymers are usually slightly more transmissive than metals are reflective). The net effect of this is, as for the aforementioned phenomena, beyond the scope of this paper, but is a problem that warrants further research.

6.3. Self-shadowing, deployment and membrane tension

Besides the optical properties of sail materials and their eventual degradation, there are other factors that contribute to in-flight losses of efficiency and model uncertainties. These pertain to the geometry of the membrane itself relative to the incident sunlight, and includes self-shadowing, wrinkling and billowing [2,12,14]. Self-shadowing occurs when a region of a solar sail partially obstructs sunlight to another region; wrinkling occurs primarily due to a localised lack of tension; and billowing occurs due to pressures acting out-of-plane to the support structures of the sail (i.e. acting along the sail normal vector $\hat{\mathbf{x}}_\mathbf{b}$).

Transmissive sails may mitigate some of these issues. Self-shadowing would be partially mitigated by the transparent nature of the sail membrane (though the scattering caused would be no-less difficult to model), and will naturally be negated if a Sun-pointing attitude is adopted. Billowing may be reduced because a significant component of the SRP generated by a transmissive sail will act in-plane with the sail support structures. Conversely, wrinkling may be helped or hindered by in-plane SRP acting with or against the sail supports in different regions; for a simple transmissive sail, the issue may be slightly exacerbated. However, tangential SRP may also be harnessed to maintain sail tension through the strategic placement and orientation of certain refractive or diffractive microstructures.

Deployment may also be aided by transmissive sail design. The deployment of large membranes requires in-plane stresses to unfold, and because refractive and diffractive microstructures can generate SRP in-plane, transmissive design may find advantage here. On the other hand, an often cited method for deploying large sails involves spin deployment (through rotation about $\hat{\mathbf{x}}_\mathbf{b}$) and the harnessing of centrifugal pseudo-forces [2]. Transmissive sails are not inherently incompatible with this, but the intent of such an approach is often to maintain tension by maintaining a high rate of spin after deployment (as for the 'heliogyro' configuration) and thereby reduce sailcraft mass by removing redundant tensile elements. This, transmissive sails *are* incompatible with, as their SRP vector will be confined to the $\hat{\mathbf{x}}_\mathbf{b}\hat{\mathbf{y}}_\mathbf{b}$ plane; the SRP vector of a spinning transmissive sail would rotate as the sail does, cancelling out any tangential component of SRP and nullifying its primary mechanism for acceleration.

6.4. Miscellaneous advantages

Transmissive sails come with some niche advantages over other sails: being transparent, they would be less prone to obstructing other systems, such as solar panels and antennas; EM waves will be scattered rather than blocked, corresponding with a reduction in power or gain rather than an outright loss of function. Conversely, strategically placed refractive or diffractive microstructures may act as a solar collector [23], increasing the power to solar cells, or even providing diffuse heating.

As well as being generally lighter than contemporary propulsion systems (corresponding with a reduced cost of launch), these LEO-capable sails may lend operators greater freedom in the choosing of their orbit due to their ability to expedite orbital decay when a satellite is disabled. At end-of-life, active attitude control cannot be assumed, and a disabled satellite will either tumble randomly or precess about $\hat{\mathbf{v}}$. Nonetheless, 'drag sails' have been shown to be effective at promoting orbital decay in the absence of active steering [73,74]. Functionally, a solar sail in LEO that is not actively steered will behave as a drag sail because F_{S_v} will tend to oscillate between positive and negative in both the tumbling case and the precession case, nullifying its effect. Conversely, the magnitude of D will librate, but its sign will not change.

Traditionally, satellites in LEO have been required to deorbit within 25 years. Recently, a 5 year rule has been adopted by the FCC [75], and by proxy, all operators who use US launch services. A sailcraft in LEO can orbit at a greater altitude than other satellites without fear of breaching these constraints; certain satellites may otherwise need to operate a drag sail to conform with these requirements. Furthermore, a sail has the additional benefit of providing a large and uniform target for any debris-capturing device. In the case of harpoon-based systems [76], a solar sail is not only easier to hit, but also comes with less risk of creating additional debris during recapture (i.e. tearing at failure rather than splintering). For laser-actuated systems [77], solar sails may be pushed into a lower or higher orbit with less precision required on the part of the laser, and without ablation needing to occur. Overall, the wide-scale adoption of transmissive sails in LEO may be instrumental in curbing the issue of space debris passively (as well as actively, see Section 5.5).

7. Conclusions

The mechanisms for transmissive solar sailing and their various designs have been discussed. Performance has been modelled for these sails with approximated α-sensitivity (informed by a custom ray-tracing optical force simulation) and γ-adaptive locally optimal steering laws for a variety of flight regimes, with a particular focus on LEO flight and the effects of atmospheric drag, eclipse and orbital precession. The results have been compared with those of similarly-modelled reflective solar sails, as well as cold gas and electric thrusters. As a breed, transmissive sails were shown to have lower sensitivity to altitude h but greater sensitivity to inclination i; they could operate at lower altitudes than reflective sails, but saw their performance disproportionately eroded at lower inclination orbits. Nonetheless, these sails often demonstrated higher performance even within low inclination orbits by merit of their peak performance being higher. The transmissive sails were then partitioned into three groups based on their performance and behaviour: (A) high performance archetypal, (B) lower performance archetypal, and (C) lower performance non-archetypal sails. Type A demonstrated the highest rate change of orbital energy $\dot{\epsilon}$, the shortest transit times $t_{h_1 \rightarrow h_2}$, and outperformed reflective sails in every flight regime. Type B was the lowest performing, and only found advantage over reflective sails at low altitudes and at inclinations near i_{SSO}. Type C were amongst the most robust, and demonstrated some of the least sensitivity to inclination i or Sun-velocity angle γ due to their large normal component to SRP, which allowed them to situationally mimic the behaviour of reflective solar sails; these also tended to outperform reflective sails in every flight regime.

When compared with thrusters, it was shown that medium-sized 36 m^2 transmissive sails performing an orbit-raising manoeuvre from a 530 km SSO generated comparable rates of acceleration to mid-range electric thrusters, but were outclassed in this respect by Hall effect and cold gas thrusters. The sensitivity of the $t_{530 \rightarrow h_2}$ of a Type A transmissive sail to i was shown to be substantial — for example, differing by up to 440% between $i = 30°$ and $i = i_{\text{SSO}}$, with failure to escape the atmosphere at $i = 0°$. Naturally, thruster transit times were independent of inclination.

Based on the theoretical performance alone, transmissive sails are suggested to be valid solutions for modern satellites completing a variety of missions in LEO and beyond; these demonstrate greater operational flexibility than their reflective peers, and are suitable for a wider range of flight regimes. However, there still exist flight regimes for which only thrusters are suitable — particularly low inclination, very low altitude orbits. In the short term, Type B and C solar sails may provide an inexpensive, high ΔV system for escaping Earth's atmosphere; in the medium term, Type A or C (meta)sails may be used for contemporary satellite applications, and may enable edge-of-the-envelope missions such as reusable space debris mitigation. The adoption of these sails over thrusters for contemporary LEO applications may be encouraged due to their ability to passively deorbit defunct satellites, the growing issue of space debris, and the narrowing window of time allowed for satellites to deorbit [75]. In the long term, ISAM may enable solar sails of arbitrary size to be fabricated in space [1]; these sails may be able to out-accelerate chemical thrusters (which see depreciating gains when increasing their size, as described by the *Tsiolkovsky rocket equation*). Very large sails or swarms of smaller sails could be used for applications ranging from manned interplanetary flight to asteroid towing. The practical advantages and limiting factors for the introduction of transmissive solar sails were also discussed, with several requiring further research — particularly the suitability of metamaterials and the optical degradation of non-metallised optical films in space.

CRediT authorship contribution statement

Samuel M. Thompson: Conceptualization, Methodology, Software, Writing – original draft, Writing – review & editing. **Nishanth Pushparaj:** Supervision. **Chantal Cappelletti:** Supervision.

Declaration of competing interest

The authors declare that they have no known competing financial interests or personal relationships that could have appeared to influence the work reported in this paper.

Acknowledgements

Samuel Thompson acknowledges the support of the Engineering and Physical Sciences Research Council (EPSRC) for funding his PhD research project.

References

[1] E. Sacco, S.K. Moon, Additive manufacturing for space: status and promises, Int. J. Adv. Manuf. Technol. 105 (10) (2019) 4123–4146, http://dx.doi.org/10.1007/s00170-019-03786-z.

[2] B. Fu, E. Sperber, F. Eke, Solar sail technology—A state of the art review, Prog. Aerosp. Sci. 86 (2016) 1–19, http://dx.doi.org/10.1016/j.paerosci.2016.07.001.

[3] S. Hassanpour, C.J. Damaren, Collocated attitude and vibrations control for square solar sails with tip vanes, Acta Astronaut. 166 (October 2018) (2020) 482–492, http://dx.doi.org/10.1016/j.actaastro.2019.07.038.

[4] A.J. Westfall, Design of an attitude control system for spin-axis control of a 3U CubeSat, 2015, http://dx.doi.org/10.31979/etd.u6fr-6t4m.

[5] A.D. Pathak, S. Saha, V.K. Bharti, M.M. Gaikwad, C.S. Sharma, A review on battery technology for space application, J. Energy Storage 61 (2023) 106792, http://dx.doi.org/10.1016/j.est.2023.106792.

[6] P.D. Fieseler, A method for solar sailing in a low earth orbit, Acta Astronaut. 43 (9–10) (1998) 531–541, http://dx.doi.org/10.1016/S0094-5765(98)00175-1.

[7] G. Mengali, A.A. Quarta, Near-optimal solar-sail orbit-raising from low earth orbit, J. Spacecr. Rockets 42 (5) (2005) 954–958, http://dx.doi.org/10.2514/1.14184.

[8] J. Behrens, Global Trends in Small Satellites, Tech. rep., 2017, URL https://www.researchgate.net/publication/335429689.

[9] M.N. Sweeting, Modern small satellites-changing the economics of space, Proc. IEEE 106 (3) (2018) 343–361, http://dx.doi.org/10.1109/JPROC.2018.2806218.

[10] R.L. Walterscheid, Solar cycle effects on the upper atmosphere: Implications for satellite drag, J. Spacecr. Rockets 26 (6) (1989) 439–444, http://dx.doi.org/10.2514/3.26089.

[11] O.L. Starinova, M.A. Rozhkov, B. Alipova, I.V. Chernyakina, Modeling the process of optical characteristics variation for a solar sail surface during heliocentric flights, J. Phys. Conf. Ser. 1368 (2) (2019) http://dx.doi.org/10.1088/1742-6596/1368/2/022036.

[12] G. Vulpetti, D. Apponi, X. Zeng, C. Circi, Wrinkling analysis of solar-photon sails, Adv. Space Res. 67 (9) (2021) 2669–2687, http://dx.doi.org/10.1016/j.asr.2020.07.016, Solar Sailing: Concepts, Technology, and Missions II.

[13] L. Niccolai, A.A. Quarta, G. Mengali, Trajectory approximation of a solar sail with constant pitch angle and optical degradation, IEEE Trans. Aerosp. Electron. Syst. 58 (4) (2022) 3643–3649, http://dx.doi.org/10.1109/TAES.2021.3124867.

[14] L. Boni, M. Bassetto, L. Niccolai, G. Mengali, A.A. Quarta, C. Circi, R.C. Pellegrini, E. Cavallini, Structural response of Helianthus solar sail during attitude maneuvers, Aerosp. Sci. Technol. 133 (2023) 108152, http://dx.doi.org/10.1016/j.ast.2023.108152.

[15] L. Niccolai, A. Anderlini, G. Mengali, A.A. Quarta, Effects of optical parameter measurement uncertainties and solar irradiance fluctuations on solar sailing, Adv. Space Res. 67 (9) (2021) 2784–2794, http://dx.doi.org/10.1016/j.asr.2019.11.037, Solar Sailing: Concepts, Technology, and Missions II.

[16] A. Caruso, L. Niccolai, A.A. Quarta, G. Mengali, Role of solar irradiance fluctuations on optimal solar sail trajectories, J. Spacecr. Rockets 57 (5) (2020) 1098–1102, http://dx.doi.org/10.2514/1.A34709.

[17] J. Mahaney, E.A. Thornton, Self-shadowing effects on the thermal-structural response of orbiting trusses, J. Spacecr. Rockets 24 (4) (1987) 342–348, http://dx.doi.org/10.2514/3.25922.
[18] L. Carzana, P. Visser, M.J. Heiligers, Solar-sail control laws for perturbed Earth-bound trajectories, in: 72nd Int. Astronaut. Conf., 2021, URL https://pure.tudelft.nl/ws/portalfiles/portal/104389460/IAC_21C135x65648.pdf.
[19] C. Bianchi, L. Niccolai, G. Mengali, M. Ceriotti, Preliminary design of a space debris removal mission in LEO using a solar sail, Adv. Space Res. 73 (8) (2024) 4254–4268, http://dx.doi.org/10.1016/j.asr.2024.01.024.
[20] M. Swartwout, The first one hundred CubeSats : A statistical look, J. Small Satell. 2 (2) (2013) 213–233, URL https://www.jossonline.com/storage/2014/12/0202-The-First-One-Hundred-Cubesats.pdf.
[21] B. Vatankhahghadim, C.J. Damaren, Solar sail deployment dynamics, Adv. Space Res. 67 (9) (2021) 2746–2756, http://dx.doi.org/10.1016/j.asr.2020.03.029, Solar Sailing: Concepts, Technology, and Missions II.
[22] P. Seefeldt, A stowing and deployment strategy for large membrane space systems on the example of Gossamer-1, Adv. Space Res. 60 (6) (2017) 1345–1362, http://dx.doi.org/10.1016/j.asr.2017.06.006.
[23] S. Firuzi, S. Gong, Refractive sail and its applications in solar sailing, Aerosp. Sci. Technol. 77 (2018) 362–372, http://dx.doi.org/10.1016/j.ast.2018.03.016.
[24] A.B. Artusio-Glimpse, The realization and study of optical wings, 2016, URL https://repository.rit.edu/cgi/viewcontent.cgi?article=10377&context=theses.
[25] G.A. Swartzlander, Radiation pressure on a diffractive sailcraft, 2017, pp. 25–30, http://dx.doi.org/10.1364/josab.34.000c25, arXiv 34 (6).
[26] G.A. Swartzlander, Flying on a rainbow: A solar-driven diffractive sailcraft, JBIS - J. Br. Interplanet. Soc. 71 (4) (2018) 130–132, http://dx.doi.org/10.48550/arXiv.1805.05864.
[27] G.A. Swartzlander, Theory of radiation pressure on a diffractive solar sail, J. Opt. Soc. Amer. B 39 (9) (2022) 2556, http://dx.doi.org/10.1364/josab.468588, arXiv:2206.10052.
[28] M. Bassetto, A. Caruso, A.A. Quarta, G. Mengali, Optimal steering law of refractive sail, Adv. Space Res. 67 (9) (2019) 2855–2864, http://dx.doi.org/10.1016/j.asr.2019.10.033.
[29] S. Firuzi, Y. Song, S. Gong, Gradient-index solar sail and its optimal orbital control, 2019, pp. 1–11, http://dx.doi.org/10.1016/j.ast.2021.107103, arXiv arXiv:1905.10977.
[30] Y. Chu, S. Firuzi, S. Gong, Controllable liquid crystal diffractive sail and its potential applications, Acta Astronaut. 182 (February) (2021) 37–45, http://dx.doi.org/10.1016/j.actaastro.2021.02.003.
[31] M. Alonso, E. Finn, Fundamental University Physics.—Vol. III: Quantum and Statistical Physics, Addison-Wesley, 1970, http://dx.doi.org/10.1063/1.3035704.
[32] C. Baxter, R. Loudon, Radiation pressure and the photon momentum in dielectrics, J. Modern Opt. 57 (10) (2010) 830–842, http://dx.doi.org/10.1080/09500340.2010.487948.
[33] C. McInnes, Solar Sailing: Technology, Dynamics and Mission Applications, in: Astronomy and Planetary Sciences, Springer, 2004, http://dx.doi.org/10.1007/978-1-4471-3992-8.
[34] E. Aspnes, T.D. Milster, K. Visscher, Optical force model based on sequential ray tracing, Appl. Opt. 48 (9) (2009) 1642–1650, http://dx.doi.org/10.1364/AO.48.001642.
[35] D. Zola, C. Circi, G. Vulpetti, S. Scaglione, Photon momentum change of quasi-smooth solar sails, J. Opt. Soc. Amer. A 35 (8) (2018) 1261–1271, http://dx.doi.org/10.1364/JOSAA.35.001261.
[36] R. Georgevic, Mathematical model of the solar radiation force and torques acting on the components of a spacecraft, 1971, pp. 33–494, URL https://ntrs.nasa.gov/citations/19720004068.
[37] O. Montenbruck, P. Steigenberger, U. Hugentobler, Enhanced solar radiation pressure modeling for Galileo satellites, J. Geod. 89 (3) (2015) 283–297, http://dx.doi.org/10.1007/s00190-014-0774-0.
[38] L. Niccolai, A.A. Quarta, G. Mengali, Analytical solution of the optimal steering law for non-ideal solar sail, Aerosp. Sci. Technol. 62 (2017) 11–18, http://dx.doi.org/10.1016/j.ast.2016.11.031.
[39] K. Oguri, G. Lantoine, Indirect trajectory optimization via solar sailing primer vector theory: Minimum solar-angle transfers, Acta Astronaut. 211 (2023) 405–415, http://dx.doi.org/10.1016/j.actaastro.2023.06.032.
[40] L. Carzana, P. Visser, J. Heiligers, Locally optimal control laws for Earth-bound solar sailing with atmospheric drag, Aerosp. Sci. Technol. 127 (2022) http://dx.doi.org/10.1016/j.ast.2022.107666.
[41] Z.J. Zhou, N.N. Yan, A survey of numerical methods for convection-diffusion optimal control problems, J. Numer. Math. 22 (1) (2014) 61–85, http://dx.doi.org/10.1515/jnum-2014-0003.
[42] S. Narayanaswamy, C.J. Damaren, Equinoctial Lyapunov control law for low-thrust rendezvous, J. Guid. Control Dyn. 46 (4) (2023) 781–795, http://dx.doi.org/10.2514/1.G006662.
[43] L. Niccolai, A.A. Quarta, G. Mengali, Solar sail heliocentric transfers with a Q-law, Acta Astronaut. 188 (2021) 352–361, http://dx.doi.org/10.1016/j.actaastro.2021.07.037.
[44] G. Swartzlander, Diffractive solar sails could outperform reflective-metal-coated sails, 2018, pp. 35–38, (October 2017). URL https://www.laserfocusworld.com/optics/article/16548235/space-and-astronomy-diffractive-solar-sails-could-outperform-reflective-metal-coated-sails.
[45] P.R. Srivastava, Y.-J.L. Chu, G.A. Swartzlander, Stable diffractive beam rider, Opt. Lett. 44 (12) (2019) 3082, http://dx.doi.org/10.1364/ol.44.003082.
[46] Y.-j.L. Chu, Measurements of Radiation Pressure on Diffractive Films, Rochester Institute of Technology, 2021, URL https://repository.rit.edu/theses/10938/.
[47] G.A. Swartzlander, T.J. Peterson, A.B. Artusio-Glimpse, A.D. Raisanen, Stable optical lift, Nat. Photonics 5 (1) (2011) 48–51, http://dx.doi.org/10.1038/nphoton.2010.266.
[48] K. Achouri, O.V. Cespedes, C. Caloz, Solar 'meta-sails' for agile optical force control, IEEE Trans. Antennas and Propagation 67 (11) (2019) 6924–6934, http://dx.doi.org/10.1109/TAP.2019.2925279.
[49] A. Ashkin, Forces of a single-beam gradient laser trap on a dielectric sphere in the ray optics regime, Biophys. J. 61 (2) (1992) 569–582, http://dx.doi.org/10.1016/S0006-3495(92)81860-X.
[50] P. Zhang, S. Firuzi, C. Yuan, X. Gong, S. Gong, General passive stability criteria for a Sun-pointing attitude using the metasurface sail, Aerosp. Sci. Technol. 122 (2022) 107380, http://dx.doi.org/10.1016/j.ast.2022.107380.
[51] J.A. Storch, Aerodynamic disturbances on rapidly rotating spacecraft in free-molecular flow, in: Eng. Constr. Oper. Challenging Environ. Earth Sp. 2004 Proc. Ninth Bienn. ASCE Aerosp. Div. Int. Conf., Vol. 2003, 2004, pp. 429–436, http://dx.doi.org/10.1061/40722(153)60, (3397).
[52] L. Casalino, A. Forestieri, Approximate optimal LEO transfers with J2 perturbation and dragsail, Acta Astronaut. 192 (2022) 379–389, http://dx.doi.org/10.1016/j.actaastro.2021.12.006.
[53] S. M, Computation of eclipse time for low-earth orbiting small satellites, Int. J. Aviat. Aeronaut. Aerosp. (2019) http://dx.doi.org/10.15394/ijaaa.2019.1412.
[54] G.J. Ward, F.M. Rubinstein, R.D. Clear, A ray tracing solution for diffuse inter-reflection, in: Proc. 15th Annu. Conf. Comput. Graph. Interact. Tech. SIGGRAPH 1988, Vol. 22, 1988, pp. 85–92, http://dx.doi.org/10.1145/54852.378490, (4).
[55] R-800 hall thruster datasheet, 2023, URL https://satsearch.co/products/rafael-r-800-hall-thruster.
[56] IFM nano thruster se / cots + datasheet, 2023, URL https://enpulsion.com/wp-content/uploads/ENP2019-086.B-IFM-Nano-Thruster-COTS-Product-Overview-1.pdf.
[57] 100 MN HPGP thruster datasheet, 2023, URL https://www.satcatalog.com/component/100mn-hpgp/.
[58] Pale blue water ion thruster 1U datasheet, 2023, https://satcatalog.s3.amazonaws.com/components/1220/SatCatalog_-_Pale_Blue_-_Water_Ion_Thruster_-_Datasheet.pdf?lastmod=20230531084516.
[59] R. Wilken, A. Holländer, J. Behnisch, Vacuum ultraviolet photolysis of polyethylene, polypropylene, and polystyrene, Plasmas Polym. 7 (2) (2002) 185–205, http://dx.doi.org/10.1023/A:1016247524912.
[60] C.P. Ennis, R.I. Kaiser, Mechanistical studies on the electron-induced degradation of polymers: Polyethylene, polytetrafluoroethylene, and polystyrene, Phys. Chem. Chem. Phys. 12 (45) (2010) 14884–14901, http://dx.doi.org/10.1039/c0cp00493f.
[61] D.W. Van Krevelen, Properties of Polymers: Their Correlation with Chemical Structure; their Numerical Estimation and Prediction from Additive Group Contributions: Fourth Edition, 2009, pp. 1–1004, http://dx.doi.org/10.1016/C2009-0-05459-2.
[62] Y. Liu, J.K. Boyles, J. Genzer, M.D. Dickey, Self-folding of polymer sheets using local light absorption, Soft Matter 8 (2012) 1764–1769, http://dx.doi.org/10.1039/C1SM06564E.
[63] G.S. Martins, I.M. Pereira, R.L. Oréfice, Toughening brittle polymers with shape memory polymers, Polymer 135 (2018) 30–38, http://dx.doi.org/10.1016/j.polymer.2017.12.017.
[64] D.C. Ullery, S. Soleymani, A. Heaton, J. Orphee, L. Johnson, R. Sood, P. Kung, S.M. Kim, Strong solar radiation forces from anomalously reflecting metasurfaces for solar sail attitude control, Sci. Rep. 8 (1) (2018) 1–11, http://dx.doi.org/10.1038/s41598-018-28133-2.
[65] B. Putz, S. Wurster, T. Edwards, B. Völker, G. Milassin, D. Többens, C. Semprimoschnig, M. Cordill, Mechanical and optical degradation of flexible optical solar reflectors during simulated low earth orbit thermal cycling, Acta Astronaut. 175 (2020) 277–289, http://dx.doi.org/10.1016/j.actaastro.2020.05.032.
[66] G.F. Abdelal, N. Abuelfoutouh, A. Hamdy, A. Atef, Thermal fatigue analysis of small-satellite structure, Int. J. Mech. Mater. Des. 3 (2006) 145–159, http://dx.doi.org/10.1007/s10999-007-9019-1.
[67] W. Saylor, Space Radiation Guide, vol. 62, 1962, URL https://www.osti.gov/biblio/4728733.
[68] N. Meyer-Vernet, Basics of the Solar Wind, Cambridge University Press, 2007, http://dx.doi.org/10.1017/CBO9780511535765.
[69] R.Y. Kezerashvili, G.L. Matloff, Solar radiation and the beryllium hollow-body sail-1 - the ionization and disintegration effects, J. Br. Interplanet. Soc. 60 (2007) 169–179, URL https://ui.adsabs.harvard.edu/abs/2007JBIS...60..169K.
[70] R.Y. Kezerashvili, Solar sail: Materials and space environmental effects, 2013, http://dx.doi.org/10.1007/978-3-642-34907-2_36, arXiv.org.
[71] C. Giori, T. Yamauchi, Space radiation resistant transparent polymeric materials, NASA - Natl. Aeronaut. Space Adm. (1977) URL https://ntrs.nasa.gov/citations/19780009276.
[72] A. El-Hameed, Radiation effects on composite materials used in space systems: a review, NRIAG J. Astron. Geophys. 11 (2022) 313–324, http://dx.doi.org/10.1080/20909977.2022.2079902.

[73] V. Tarantini, G. Bonin, R. Zee, De-orbit analysis of a tumbling sailcraft, in: Proceedings of the Small Satellites Systems and Services Symposium, Porto Perto, 2014.
[74] Z. Serfontein, J. Kingston, S. Hobbs, I.E. Holbrough, J.C. Beck, Drag augmentation systems for space debris mitigation, Acta Astronaut. 188 (2021) 278–288, http://dx.doi.org/10.1016/j.actaastro.2021.05.038.
[75] W. Wiquist, FCC adopts new '5-year rule' for deorbiting satellites, 2022, URL https://www.fcc.gov/document/fcc-adopts-new-5-year-rule-deorbiting-satellites.
[76] J. Hsu, Fishing for space junk, IEEE Spectr. 55 (6) (2018) 7–9, http://dx.doi.org/10.1109/MSPEC.2018.8362211.
[77] C.R. Phipps, LADROIT - A spaceborne ultraviolet laser system for space debris clearing, Acta Astronaut. 104 (1) (2014) 243–255, http://dx.doi.org/10.1016/j.actaastro.2014.08.007.